

Vacancy defects in semiconductor materials
for opto and spin electronics

Filip Tuomisto

*Laboratory of Physics
Helsinki University of Technology
Espoo, Finland*

Dissertation for the degree of Doctor of Science in Technology to be presented with due permission of the Department of Engineering Physics and Mathematics for public examination and debate in Auditorium E at Helsinki University of Technology (Espoo, Finland) on the 14th of October, 2005, at 13 o'clock.

Dissertations of Laboratory of Physics, Helsinki University of Technology
ISSN 1455-1802

Dissertation 134 (2005):
Filip Tuomisto: Vacancy defects in semiconductor materials for opto and spin
electronics
ISBN 951-22-7823-5 (print)
ISBN 951-22-7824-3 (electronic)

Otamedia OY
ESPOO 2005

Abstract

The vacancy defects in GaN, ZnO and (Ga,Mn)As have been studied by positron annihilation spectroscopy. We show that both the thermodynamical quantities and the kinetics of the growth have a significant impact on impurity incorporation and point defect formation in all three materials. In addition the incorporation and stability of point defects in electron irradiated ZnO is studied.

In GaN the Ga vacancies and vacancy clusters are more abundant at the N polar side. The concentrations of oxygen and of acceptor-type impurities are similarly correlated with the polarity. The vacancy concentrations are similar in both HVPE and high-pressure grown GaN in spite of the much higher growth temperature of the latter. This suggests that the thermal stability of the point defect complexes is an important factor determining which defects survive the cooling down from the growth temperature.

The Zn vacancy is shown to be the dominant intrinsic acceptor in undoped ZnO. Vacancies on both sublattices and negative ion type defects are produced in electron irradiation, and their concentrations are determined. In addition, the irradiation-induced Zn vacancies have an ionization level close to 2.3 eV, hence it is likely that they are involved in the transition responsible for the green luminescence in ZnO. The irradiation-induced point defects fully recover after the annealing at 600 K. The Zn vacancies anneal out of the material in two stages, indicating that the Zn vacancies are parts of two different defect complexes. The O vacancies anneal simultaneously with the Zn vacancies at the later stage. The negative ion type defects anneal out between the two annealing stages of the Zn vacancies.

The Zn vacancies are the dominant defects observed by positrons in thin heteroepitaxial ZnO layers. Their concentration depends on the surface plane of sapphire over which the ZnO layer has been grown. There is a correlation between the misorientation of the sapphire surface planes and the concentration of the vacancies for layers with thickness at most 500 nm. In addition to the misorientation, the defect content in the layer depends on the layer thickness.

The concentrations of both native As antisites (donors) and Ga vacancies (acceptors) vary as a function of the Mn content in (Ga,Mn)As, following thermodynamic trends, but the absolute concentrations are determined by the growth kinetics and stoichiometry.

Preface

This thesis has been prepared in the Positron Group in the Laboratory of Physics at the Helsinki University of Technology during the years 2002-2005. I am grateful to Prof. Pekka Hautojärvi for giving me the opportunity to work in this experimental group.

I am indebted to Prof. Kimmo Saarinen for the excellent guidance and supervision he has provided during the time I have been in the laboratory. This thesis wouldn't exist without his infectious enthusiasm for physics. I am also glad to thank Prof. Tadeusz Suski for the opportunity to visit Unipress on several occasions and for all the arrangements during my family's stays in Warsaw. Our scientific collaboration has been most fruitful.

I wish to thank the members of the positron group, both current and former, for creating a pleasant and inspiring working environment. Further thanks go to the electronic properties of materials group led by Prof. Martti Puska for all the valuable conversations concerning theoretical calculations. Also the help from the administrative staff and the skillful people at the electronic and mechanical workshops is gratefully appreciated. I also wish to thank all my collaborators that have made finishing of this thesis possible, both from the local positron group and institutes abroad, including the Polish Academy of Sciences, the Warsaw University, the Warsaw University of Technology, the Radboud University Nijmegen, VTT, the Wright State University, the University of the Basque Country, CNRS, and the University of Valencia.

The financial support from the Emil Aaltonen foundation, Jenny and Antti Wihuri foundation, the Research Foundation of Helsinki University of Technology and the Finnish Cultural Foundation is gratefully acknowledged.

My parents and grandparents have supported me throughout my whole life and taught me to be proud of my achievements. My little sisters deserve huge hugs for putting up with me for all these years.

Finally, I want to thank my wife Noora and my son Oskari for not letting me forget what's really important in life. I wouldn't be here without You two.

Espoo, August 2005

Filip Tuomisto

Contents

Abstract	i
Preface	ii
Contents	iii
List of publications	iv
1 Introduction	1
2 Experimental methods	5
2.1 Optical methods	5
2.2 Positron annihilation spectroscopy	7
2.3 Low temperature proton irradiation facility	14
3 Wide bandgap semiconductors for optoelectronics	16
3.1 Gallium nitride (GaN)	17
3.2 Zinc Oxide (ZnO)	22
4 Magnetically doped semiconductors for spin electronics	35
4.1 Gallium arsenide (GaAs) doped with Mn	36
4.2 Future: Doping of GaN and ZnO with Mn	39
5 Summary	40
Bibliography	42

List of publications

This thesis consists of an overview and the following publications:

- I** F. Tuomisto, T. Suski, H. Teisseyre, M. Kryśko, M. Leszczyński, B. Łucznik, I. Grzegory, S. Porowski, D. Wasik, A. Witowski, W. Gębicki, P. Hageman, and K. Saarinen, *Polarity dependent properties of GaN layers grown by hydride vapor phase epitaxy on GaN bulk crystals*, physica status solidi (b) **240**, 289–292 (2003).
- II** F. Tuomisto, K. Saarinen, T. Suski, H. Teisseyre, B. Łucznik, I. Grzegory, P. Hageman, and J. Likonen, *Effect of growth polarity on vacancy defect and impurity incorporation in dislocation-free GaN*, Applied Physics Letters **86**, 031915:1–3 (2005).
- III** F. Tuomisto, V. Ranki, K. Saarinen, and D. C. Look, *Evidence of the Zn Vacancy Acting as the Dominant Acceptor in n-Type ZnO*, Physical Review Letters **91**, 205502:1–4 (2003).
- IV** F. Tuomisto, K. Saarinen, D. C. Look, and G. C. Farlow, *Introduction and recovery of point defects in electron-irradiated ZnO*, Physical Review B **72**, 085206:1–11 (2005).
- V** A. Zubiaga, F. Tuomisto, F. Plazaola, K. Saarinen, J. A. Garcia, J. F. Rommeluere, J. Zuñiga-Pérez, and V. Muñoz-San José, *Zinc vacancies in the heteroepitaxy of ZnO on sapphire: influence of the substrate orientation and thickness*, Applied Physics Letters **86**, 042103:1–3 (2005).
- VI** F. Tuomisto, K. Pennanen, K. Saarinen, and J. Sadowski, *Ga Sublattice Defects in (Ga,Mn)As: Thermodynamical and Kinetic Trends*, Physical Review Letters **93**, 055505:1–4 (2004).

The author has had an active role in all the phases of the research reported in this thesis. He has had an active role in the planning and performing of the experiments as well as in the analysis of experimental data, and he has contributed significantly to the interpretation of the results. The author has written Publications I – IV and VI, and the work in Publication V was performed under the author’s guidance.

Chapter 1

Introduction

Semiconductor materials form the basis of modern electronics and optoelectronics. The essential property of these materials is that their electrical conductivity can be tuned over several orders of magnitude by the addition of impurities to the crystal lattice. The electrical carriers may be either negative (electrons) as in metals or positive (holes). Due to the forbidden energy gap (also called the band gap) the interactions of these carriers with external electromagnetic fields, such as light, are numerous, making the materials optically active.

Light emitting diodes (LEDs) are much more efficient than conventional light bulbs, since practically all of the energy can be converted to electromagnetic radiation in the visible wavelengths. In order to produce white light for everyday use, LEDs in the blue region are needed. Due to their shorter wavelength, blue and ultraviolet (UV) semiconductor lasers can be used for more effective optical data storage on new types of compact and digital video disks. For the semiconductor light emitting devices to emit in the blue to UV spectral region, semiconductor materials with a wide band gap are needed. These same materials could also be used in electronic devices that need to work in high temperatures, since the wide band gap minimizes the leakage currents. Gallium nitride (GaN) and zinc oxide (ZnO) are two structurally similar materials that have a band gap of about 3.4 eV, suitable for the above-mentioned purposes.

The use of spin information in addition to charge in electronics has recently become a widely researched topic. An important issue in spin electronics is the injection of spins into the electronic devices, which is most efficient if the semiconductor material itself is ferromagnetic. Injection of spin-polarized current from a metal is very difficult and the efficiency is poor. Possible future devices making use of the spin information are super-fast field effect transistors or even quantum computers. Ferromagnetic semiconductors can be produced by doping the

conventional semiconductors with transition metals, such as manganese (Mn) or cobalt (Co). One of the most studied materials is GaAs doped with Mn, due to the well-known properties of GaAs itself.

Since the control of conductivity is performed by adding impurities to the semiconductor material, lattice imperfections are a critical issue. These include both intentional and unintentional impurities, intrinsic point defects such as vacancies and interstitials, and defects of higher dimensionality such as dislocations. The point defects can act as compensating centers that deactivate intentionally incorporated donor or acceptor impurities. They can also be optically active and act as either radiative or non-radiative recombination centers thus affecting the optical properties of the material. In order to produce materials of high quality, it is imperative to understand and control the formation of the point defects, and how post-growth processing affects them.

The formation of point defects in semiconductor materials is governed by both the thermodynamics and kinetics during growth and cooling down. The main thermodynamical quantity is the formation energy of the particular defect. The defect in question need not be isolated, it can also be a complex of different point defects, such as a vacancy-impurity pair. The stability of the particular defect is important, since often the point defects are mobile at the typical growth temperatures of several hundred Kelvin. The migration barrier of the defect determines the temperature at which the point defect “freezes”, and thus the cooling down process is important. In the case of defect complexes, the binding energy of the complex is another important quantity in addition to the migration barrier of the isolated defect. The growth process itself is often far from being in thermal equilibrium. Various aspects related to growth kinetics affect the impurity and defect incorporation. The direction in which the growth proceeds, *i.e.* which lattice planes are perpendicular to the growth direction, has a critical impact on the incorporation of impurities. Especially in the case of compound semiconductors, the partial pressures of the two constituents have an important effect in determining the sublattice of the majority of the point defects.

In this thesis the formation and annealing of mostly cation sublattice vacancy defects is studied in GaN, ZnO and (Ga,Mn)As. The thermodynamical and kinetic trends are examined both in the case of in-grown and irradiation-induced defects. To do this, we have used positron annihilation spectroscopy (PAS). It is a powerful tool providing unambiguous identification of vacancy-type defects. It gives information on the atomic structure, charge state and concentration of the defects. By combining this method with optical and electrical measurements quantitative studies of electrical compensation and optical properties can be conducted. PAS is based on the detection of the radiation produced in the annihilation of positrons with the electrons of the sample material. Prior to annihilation, positrons can get

trapped at neutral or negative vacancy defects, which changes their annihilation characteristics.

In Publs. I and II we have studied GaN grown by hydride vapor phase epitaxy (HVPE) on both polarity faces of high pressure (HP) grown bulk GaN crystals. We show that the material grown on the N polar side of GaN single crystals has a high crystallographic quality but reproduces also the rather poor optical properties of the bulk GaN substrate. On the other hand, the layers grown on the Ga polar side combine the structural quality of the bulk crystal with excellent optical properties. With PAS we demonstrate that the growth polarity has a crucial impact on the formation of Ga vacancies and vacancy clusters, which are more abundant at the N polar side. The concentrations of oxygen and of acceptor-type impurities are similarly correlated with the polarity. The vacancy concentrations are similar in both HVPE and high-pressure grown GaN in spite of the much higher growth temperature of the latter, which suggests that the stability of the point defect complexes is an important factor determining which defects survive the cooling down from the growth temperature.

In Publs. III and IV we have studied bulk ZnO crystals grown by a seeded vapor phase method. By combining PAS with temperature-dependent Hall measurements we show that the Zn vacancy is the dominant intrinsic acceptor in undoped ZnO. We show that 2-MeV electron irradiation at room temperature produces vacancies on both sublattices and negative ion type defects, tentatively identified as O interstitials. The Zn vacancies and the negative ions act as compensating centers, both produced at concentrations $[V_{\text{Zn}}] \simeq c_{\text{st}} \simeq 2 \times 10^{16} \text{ cm}^{-3}$. The irradiation-induced O vacancies are deep donors with the ionization level about 100 meV below the conduction band, and produced at a concentration of $[V_{\text{O}}] \simeq 3 \times 10^{17} \text{ cm}^{-3}$. The lifetime of a positron trapped at an O vacancy is determined to be $\tau_{V,\text{O}} = 195 \pm 5 \text{ ps}$, while it is $\tau_{V,\text{Zn}} = 230 \pm 10 \text{ ps}$ in the Zn vacancy. By shining monochromatic light on the samples during the positron annihilation measurements at low temperature, we find that both the irradiations-induced Zn vacancies and the negative ion type defects have ionization levels close to 2.3 eV. Since the Zn vacancies have the lowest defect formation energy in *n*-type ZnO, it is likely that they are involved in the transition responsible for the green luminescence in ZnO.

The irradiation-induced defects fully recover after the annealing at 600 K, in good agreement with electrical measurements. The Zn vacancies anneal out of the material in two stages with fitted activation energies $E_{A1}^{V,\text{Zn}} \simeq 1.3 \text{ eV}$ and $E_{A2}^{V,\text{Zn}} \simeq 1.8 \text{ eV}$, indicating that the Zn vacancies are parts of two different defect complexes. The O vacancies anneal simultaneously with the Zn vacancies at the later stage with fitted activation energy $E_A^{V,\text{O}} \simeq 1.8 \text{ eV}$. The negative ion type defects anneal out between the two annealing stages of the Zn and O vacancies.

We have studied thin heteroepitaxial ZnO layers grown by metal-organic chemical vapor deposition (MOCVD) on sapphire in Publ. V. Zn vacancies are the dominant defects observed by PAS. Their concentration depends on the surface plane of sapphire over which the ZnO layer has been grown. We show a correlation between the misorientation of the sapphire surface planes and the concentration of the vacancies for layers with thickness at most 500 nm. This correlation disappears for thicker layers. Moreover, the defect content in the layer depends on the layer thickness, and is larger closer to the interface.

The native Ga sublattice defects in (Ga,Mn)As grown by low temperature molecular beam epitaxy (LT-MBE) with Mn content ranging from 0 % to 5 % were studied by infrared absorption and PAS in Publ. VI. We show that the concentrations of both As antisites (donors) and Ga vacancies (acceptors) vary as a function of the Mn content following thermodynamic trends, but the absolute concentrations are determined by the growth kinetics and stoichiometry. The As antisite concentrations ($\sim 10^{20} \text{ cm}^{-3}$) are significant for the hole compensation and magnetic properties. In addition, the presence of the Ga vacancies in the lattice may enhance the diffusion of Mn in the group III sublattice during the post-growth annealing that improves the magnetic properties of the layers.

Chapter 2

Experimental methods

Traditional defect characterization in semiconductors is conducted by electrical and optical measurements. Typical electrical methods are *e.g.* measurements of Hall resistivity or the deep level transient spectroscopy (DLTS), while typical optical methods are the photoluminescence (PL) and infrared reflectivity methods (IR). With these methods the defects are readily detected, but their structure is often unresolved. Methods based on electron paramagnetic resonance (EPR) are more sensitive to the structure of the defects, but determination of the defect concentrations is difficult. Positron annihilation spectroscopy is a powerful tool, providing unambiguous identification of vacancy-type defects. It gives information on the atomic structure, charge state and concentration. By combining this method with electrical and optical measurements quantitative studies of electrical compensation, light absorption and photoluminescence can be conducted. The optical methods used in the work presented in this thesis are briefly explained in this chapter. The principles of the positron annihilation spectroscopy are also presented. In addition, we explain the basic idea of a recently constructed low temperature proton irradiation facility. This facility is equipped with an *in situ* positron measurement system and thus enables the study of the thermal stability of point defects mobile at low temperatures.

2.1 Optical methods

The forbidden energy gap makes semiconductor materials optically active. Photons of sufficient energy can excite electrons from the filled valence bands to the empty conduction bands. Photons can also interact with lattice vibrations and electrons localized on defects. The optical processes that occur when light interacts with a medium are numerous.

At the surface of the medium, a fraction of the light is reflected and the rest transmitted. Inside the medium some of the radiation is scattered or absorbed, while the rest passes through the sample under illumination. The absorbed light is either dissipated as heat or re-emitted at a different frequency. The process of absorption and re-emission is called photoluminescence. Photons or electromagnetic waves are scattered inside the medium by inhomogeneities, which may be static (defects) or dynamic (phonons). In the work presented in this thesis, we have used four types of optical measurements: photoluminescence, Raman scattering, infrared reflectivity and infrared absorption. These techniques are briefly described in the following, more detailed presentations can be found *e.g.* in Refs. [1,2].

In photoluminescence experiments the sample is excited with a laser with energy higher than the bandgap energy, and the emitted radiation is measured as a function of energy. The excitation creates electron-hole pairs which thermalize rapidly. The emitted light is produced by the radiative recombination of these pairs. The most important radiative recombination centers are donors and acceptors, where the electrons and holes can be localized by themselves or after forming a common bound state called an exciton. Hence in a photoluminescence spectrum four different types of optical transitions are observed: band-to-band (no localization), free-to-bound (either hole or electron is localized), donor-acceptor-pair (both the hole and the electron are localized) and exciton recombination (either free or bound).

In Raman scattering experiments the sample is typically illuminated by a laser with visible wavelength. The incoming light is inelastically scattered by phonons, and thus the scattered light reflects the phonon structure of the sample. The interaction of light with the phonons occurs through the light-induced polarization, and hence the optical activity of specific phonons is determined by both the polarization and wavevector of the incoming and scattered light. By tuning the polarization of the incoming and measured light as well as the geometry of the experiment different acoustic and optical phonons can be activated and their wavelengths determined. In addition to phonons, the incoming light can interact with the so-called coupled longitudinal phonon-plasmon modes if a substantial concentration of free carriers is present. This provides a way of measuring optically the free carrier concentration.

The reflection coefficient of light at normal incidence is determined by the complex dielectric function of the material. The dielectric function contains information on the plasma frequency of the free carriers as well as the phonon frequencies of transverse and longitudinal optical phonons. Hence by fitting the theoretical reflectivity to the measured data these optical constants can be obtained. The typical plasma and phonon frequencies are such that the most interesting features

in the reflectivity of a semiconductor material occur in the infrared range.

The absorption coefficient of light is also determined by the absorption of light by the free carriers. In addition, when the energy of the incoming light coincides with the ionization energy of an optically active defect, a steep increase proportional to the defect concentration is observed in the absorption coefficient. Hence by performing the absorption measurements at sufficiently low temperatures, where the free carriers are frozen, the ionization levels and the concentrations of the optically active defects can be studied. The typical defect ionization energies are about 0.5 – 1.5 eV, making the absorption in the infrared range the most interesting.

2.2 Positron annihilation spectroscopy

Positron annihilation spectroscopy is an experimental method sensitive to defects with open volume. The method is based on the detection of the radiation produced in the annihilation of positrons with the electrons in the sample material. Prior to annihilation, positrons can get trapped at neutral or negative vacancy defects due to the missing Coulomb repulsion of the positive ion core, which changes their annihilation characteristics. At a vacancy defect the electron density is lower than elsewhere in the material, and the lifetime of a positron trapped into a vacancy is longer than that of a positron in a free state in the lattice. Thus the positron lifetime reflects the open volume of the defect. On the other hand, due to momentum conservation in the annihilation process, the energy of the annihilation photons is Doppler-shifted by the momentum of the electrons at the annihilation site. Hence the measurement of the Doppler broadening of the 511 keV annihilation line is sensitive to the atomic environment of a vacancy. The combination of these techniques can be used to identify both the open volume and the sublattice of vacancy defects in compound semiconductors. Thorough reviews on the measurement methods and the theory of positrons in solids can be found in Refs. [3–5].

2.2.1 Fast and moderated positrons

Both fast and moderated positrons can be used in the measurements. In the case of fast positrons, the positron source is sandwiched between two identical sample pieces. Due to its suitably long half-life of 2.6 years, a commonly used positron source is ^{22}Na , where the positrons are produced through the nuclear β^+ decay process with a maximum energy of 0.54 MeV. In this setup the positrons leaving the source immediately enter the sample, and hence the sample needs to be at

least a few tens of microns thick in order to stop the positrons. The positrons rapidly lose their energy first through ionization and core electron excitations, and then by electron-hole excitation and phonon emission. This thermalization process takes only a short time compared to the lifetime of the positron. Hence the positrons behave as fully thermalized particles in semiconductors and only very few positrons annihilate during the thermalization process. The thermalized positron diffuses behaving as a free carrier in the semiconductor lattice typically for a few hundred picoseconds, possibly gets trapped at a defect, and finally annihilates with an electron emitting two 511 keV photons.

If the thickness of the sample to be studied is only a few micrometers the positrons have to be moderated before they enter the material. In conventional slow positron beams this is achieved by placing a thin moderator (*e.g.* tungsten) film in front of the positron source. The vast majority of the positrons fly through the moderator without losing considerable parts of their energy, but a small fraction thermalizes and escapes from the surface due to the negative work function of the moderator material. The fast positrons are discarded with the help of an energy selector. The thermalized mono-energetic positrons are accelerated to desired energies with an electric field and the positron beam is guided to the sample with magnetic fields. The typical size of such an apparatus is a few meters, which requires a vacuum of at least 10^{-4} Pa for the positrons to reach the sample without scattering. The penetration depth of the positrons into the sample can be adjusted by controlling the accelerating electric field.

The positron emission from ^{22}Na is followed by a very rapid decay of the excited nuclear state of the resulting ^{22}Ne isotope, producing a 1.28 MeV photon. When fast positrons are used, this photon is used as the start signal in the positron lifetime measurement (the stop signal is obtained from the annihilation photon). Unfortunately the usefulness of this signal is lost in the moderation process, allowing only measurements of the Doppler broadening in thin layers when a conventional slow positron beam is used. A way to circumvent this problem is to use a pulsed positron beam, where the start signal for the lifetime measurement is obtained from the pulsing electronics.

2.2.2 Annihilation parameters

The positron lifetime measurements presented in this thesis were performed in the conventional way, where the sample-source sandwich is placed between two detectors in collinear geometry. Both detectors consist of a fast scintillator coupled to a photomultiplier tube. One of the detectors (start) is tuned to detect the 1.28 MeV photon emitted simultaneously with the positron and the other (stop) detects one of the 511 keV annihilation photons. These timing pulses, obtained

with constant-fraction discriminators, are guided to a time-to-amplitude converter which transforms their time difference to a voltage pulse with the amplitude proportional to the time difference. The pulses are collected on a computer with a multichannel analyzer and form the lifetime spectrum. Typically $1-5 \times 10^6$ pulses are collected to a single lifetime spectrum, which takes 1 – 10 hours depending on the activity of the source.

The positron lifetime spectrum is the annihilation rate of the positrons as a function of time. The probability distribution $P(t)$ of positron annihilation, *i.e.* the normalized annihilation rate, is obtained as

$$P(t)dt = d(1 - n(t)) \Rightarrow P(t) = -\frac{dn(t)}{dt}, \quad (2.1)$$

where $n(t)$ is the probability that the positron is alive at time t . $n(t)$ is obtained by solving the kinetic trapping equations of positrons. This gives

$$n(t) = \sum_{i=1}^{N+1} I_i e^{-\lambda_i t}, \quad (2.2)$$

where λ_i are the decay constants, I_i the corresponding intensities ($\sum_i I_i = 1$) obtained from the kinetic equations and N is the amount of bound positron states. The lifetime components are defined as the reciprocal values of the decay constants $\tau_i = \lambda_i^{-1}$.

A typical lifetime spectrum is presented in Fig. 2.1. The measured spectrum is a convolution of the ideal spectrum presented above and the resolution function (typical width 200 – 250 ps) of the system. In addition, a few percent of the positrons annihilate in the source material and the Al foil surrounding it, producing additional components to the experimental spectrum. For these reasons, usually at most three components can be separated in the experimental lifetime spectra, given that they differ by at least 50 % from each other. The separation is performed by fitting the convoluted theoretical lifetime spectrum to the measured data. The effect of the source components can be eliminated by measuring a defect free reference sample. On the other hand, when the resolution function is Gaussian, it does not affect the average positron lifetime defined as

$$\tau_{\text{ave}} = \int_0^\infty tP(t)dt = \sum_{i=1}^{N+1} I_i \tau_i. \quad (2.3)$$

The average positron lifetime (center of mass of the spectrum) is an important quantity since it can be accurately determined even if the decomposition of the

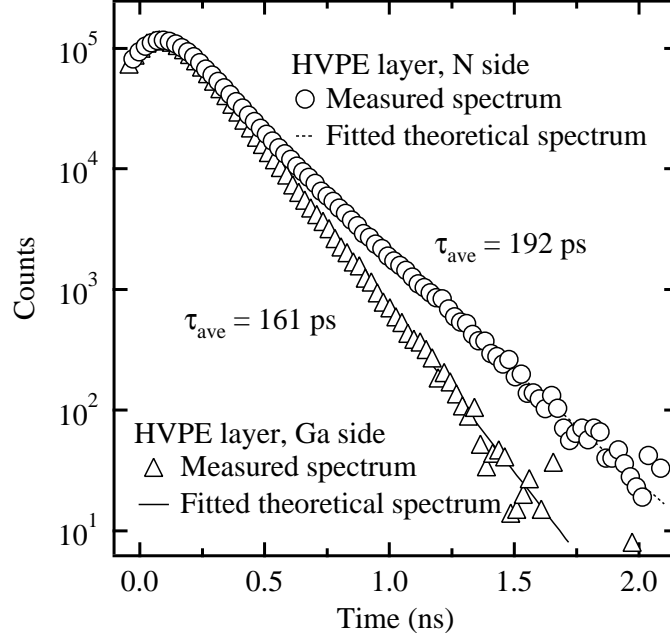


Figure 2.1: Measured and fitted positron lifetime spectra in HVPE GaN grown on the N and Ga polar sides of the single crystal GaN substrate. The Ga side spectrum is one-componential and the N side spectrum has two lifetime components.

lifetime spectrum is difficult. It can be represented with the help of fractions of annihilations at different defects $\eta_{D,j}$ and the corresponding lifetimes $\tau_{D,j}$:

$$\tau_{\text{ave}} = \left(1 - \sum_{j=1}^N \eta_{D,j}\right) \tau_B + \sum_{j=1}^N \eta_{D,j} \tau_{D,j} = \eta_B \tau_B + \sum_{j=1}^N \eta_{D,j} \tau_{D,j}, \quad (2.4)$$

where τ_B is the lifetime of a positron in the free state in the defect-free lattice. At vacancy defects $\tau_{D,j} > \tau_B$ due to the smaller electron density, and thus the increase of the average positron lifetime above τ_B indicates the presence of vacancy defects in the sample even if the different lifetime components are unknown.

In Doppler broadening experiments the observed quantity is the energy of the 511 keV photons emitted in the annihilation process. The momentum of the annihilating positron-electron pair causes a shift in this energy. Since the positrons annihilate as thermalized, their momentum can be neglected and the measured energy spectrum shows the Doppler broadening of the 511 keV annihilation line induced by the electron momentum distribution at the annihilation site. In the

work presented here, the photon energies were measured with high purity Ge detectors with energy resolutions in the range of 1.2 – 1.5 keV at 511 keV. The detector signal is amplified with a spectroscopy amplifier and stabilized digitally in order to remove the effect of instabilities in the measurement system. The pulses are collected to an energy histogram on a computer with the help of a multichannel analyzer.

The resolution of the detector is of the same order of magnitude as the Doppler broadening itself. Hence the Doppler spectrum is conventionally characterized with the shape parameters S and W (Fig. 2.2). The S parameter is the fraction of annihilations with low-momentum valence electrons (longitudinal momentum component $p_L < 3 \times 10^{-3}m_0c$) which cause a maximal shift of 0.7 keV to the photon energy. The W parameter is the fraction of annihilations with high-momentum core electrons ($10 \times 10^{-3}m_0c < p_L < 30 \times 10^{-3}m_0c$), which cause a shift in the photon energy in the range 2.6 – 7.5 keV. The annihilation of positrons as trapped at vacancy defects is typically observed as an increase of the S parameter and a decrease in the W parameter. In addition, due to its core-electron definition, the W parameter is sensitive to the chemical environment of the vacancy defect and it can be used for the detection of decoration of vacancies by impurities.

The high-momentum region of the Doppler spectrum can be studied in more detail by lowering the background level in the measurement. This can be achieved by detecting both photons emitted in the annihilation process. The angle between the emitted photons deviates only slightly from the 180° angle, and another detector in collinear geometry with the Ge detector can be used for gating the signal. The simple way to do this is to use a poor-resolution NaI scintillating detector and allowing only the addition of pulses to the Doppler spectrum when both detectors detect a photon within a specified coincidence time. In this setup the peak-to-background ratio can be improved by a factor of roughly 100 from $\sim 10^2$ to $\sim 10^4$ (Fig. 2.2). A more complex way is to use two Ge detectors for the detection of the two annihilation photons. In this setup an additional restriction can be imposed on the allowed pulses, *i.e.* the conservation of energy. The sum of the energies of the two simultaneously observed annihilation photons needs to be about $2m_0c - E_b$. This restriction improves the peak-to-background ratio by another factor of roughly 100, resulting in $\sim 10^6$, as can be seen in Fig. 2.2. In addition, the resolution of the system is improved by a factor of $\sqrt{2}$.

The coincidence measurements of the Doppler broadening provide the possibility of comparing the experimental high-momentum data to theoretical calculations. The form of the electron momentum distribution of the core region can then be analyzed and the effect of *e.g.* impurity decoration determined.

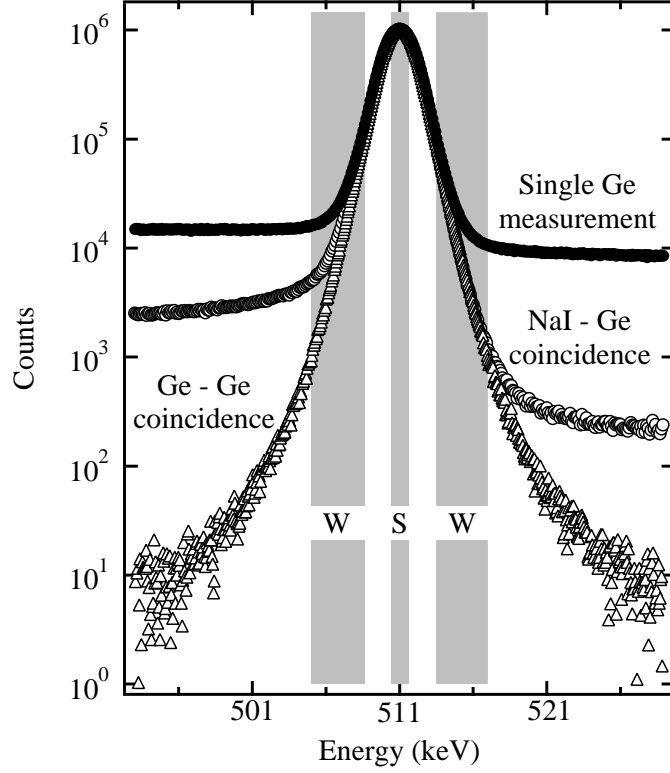


Figure 2.2: Doppler broadening spectra obtained in different data collection modes. The definition of the shape parameters S and W is shown. The data was measured in a bulk ZnO sample, where no positron trapping at defects is observed at 300 K (Pubs. III and IV)

2.2.3 Data analysis

The temperature dependence of the positron annihilation parameters (τ_{ave} , S and W) can be analyzed with the model of trapping and escape rates of positrons. In this model, the trapping coefficient μ_V to a neutral vacancy is independent of temperature and to a negatively charged vacancy it varies as $T^{-0.5}$. The trapping rate of positrons into the vacancies (concentration c_V) is $\kappa_V = \mu_V c_V$. Positrons can get trapped also at hydrogen-like Rydberg states surrounding negative ion type defects (shallow traps for positrons). The positron trapping rate at the Rydberg state μ_R varies also as $T^{-0.5}$, which is the result predicted by theory for the transition from a free state to a bound state in a Coulomb potential. The thermal escape rate from the Rydberg state can be written as

$$\delta_{\text{st}} = \mu_{\text{R}} \left(\frac{m_+ k_B T}{2\pi \hbar^2} \right)^{3/2} \exp(-E_{b,\text{st}}/k_B T), \quad (2.5)$$

where μ_{R} is the positron trapping coefficient to the lowest hydrogen-like Rydberg state, $E_{b,\text{st}}$ is the positron binding energy of the lowest Rydberg state (typically < 0.1 eV), and $m_+ \simeq m_0$ is the effective mass of the positron. Positrons can also escape from the Rydberg states around negatively charged vacancies, as observed in Si and GaAs [3]. On the other hand, the data obtained in GaN [6] suggests that the transition from the Rydberg state to the ground state in the vacancy is fast and thus the effect of the escape on the data is not important. The trapping model presented here is applied to ZnO, a material structurally very similar to GaN, and hence the escape of positrons from negatively charged vacancies will be assumed to be negligible. An effective trapping rate of the shallow traps can thus be defined as

$$\kappa_{\text{st}}^{\text{eff}} = \frac{\kappa_{\text{st}}}{1 + \delta_{\text{st}}/\lambda_{\text{st}}}, \quad (2.6)$$

where $\lambda_{\text{st}} \simeq \lambda_{\text{B}}$ is the annihilation rate of positrons trapped at the Rydberg state, which coincides with the annihilation rate λ_{B} from the delocalized state in the bulk lattice, and $\kappa_{\text{st}} = \mu_{\text{R}} c_{\text{st}}$ is directly related to the concentration of the negative ions.

The decomposition of the lifetime spectra into several lifetime components gives the possibility to determine experimentally the fractions of positrons annihilating in various states. The annihilation fractions are related to the trapping rates of different defects through

$$\eta_{\text{B}} = \frac{\lambda_{\text{B}}}{\lambda_{\text{B}} + \sum_j \kappa_{D,j}^{\text{eff}}}, \quad \eta_{D,j} = \frac{\kappa_{D,j}^{\text{eff}}}{\lambda_{\text{B}} + \sum_{j'} \kappa_{D,j'}^{\text{eff}}}. \quad (2.7)$$

Equation (2.4) can be fitted to the τ_{ave} vs. T data, using the trapping rates and the possible binding energies to the Rydberg states as fitting parameters. Another possibility is to write the trapping rate $\kappa_{D,j}^{\text{eff}}$ to a defect D_j as a function of the experimental parameters:

$$\kappa_{D,j}^{\text{eff}} = \lambda_{\text{B}} \frac{\tau_{\text{ave}} - \tau_{\text{B}}}{\tau_{D,j} - \tau_{\text{ave}}} - \sum_{j' \neq j} \kappa_{D,j'}^{\text{eff}} \frac{\tau_{D,j'} - \tau_{\text{ave}}}{\tau_{D,j} - \tau_{\text{ave}}}. \quad (2.8)$$

In the case of only one type of defect, the sum in Eq. (2.8) vanishes and the trapping rate can be calculated directly from the experimental values of τ_{ave} , $\tau_{D,j}$

and τ_B . If several defect types are present, the trapping rates to the other defects need to be known. The measured S and W parameters behave similarly as the average positron lifetime τ_{ave} , and the above analysis can be performed with the Doppler parameters as well by substituting the defect-specific lifetime components by the corresponding Doppler parameters.

2.3 Low temperature proton irradiation facility

Electron irradiation is a valuable technique to introduce basic point defects into a semiconductor material in a controlled way. The annealing treatments of the irradiated material yield important information on the thermal stability of isolated intrinsic point defects. Such knowledge can be compared with the properties of native defects present in as-grown material in order to understand their atomic structure and formation mechanisms during the growth. Irradiation by electrons has been used to produce point defects also in the work presented in this thesis (Publs. III and IV).

A typical irradiation at room temperature with 2-MeV electrons produces primary vacancy defects with an introduction rate of about 1 cm^{-1} . Irradiation with protons creates defects at a roughly 2000 times faster rate due to the higher mass of the particle. However, the produced defects have been observed to be the same in both irradiations [7–9], primarily monovacancies. Hence protons can be used instead of electrons in irradiation experiments. The advantage is that a lower fluence is needed due to the faster introduction rate. On the other hand, clearly higher particle energy is needed for the protons to obtain a homogeneous defect profile along the proton track.

In some materials the primary defects produced in the irradiation are mobile already at room temperature and disappear after the irradiation. Thus valuable information is lost if the irradiation is performed at room temperature. To solve this problem, we have designed a low-temperature proton irradiation facility with an *in situ* fast positron measurement system in collaboration with the Accelerator laboratory of the University of Helsinki. The schematic design is shown in Fig. 2.3. 10 MeV protons are obtained from the 5 MV EGP 10-II Tandem Accelerator and guided to the positron measurement chamber equipped with a closed-cycle cryostat enabling irradiation and measurements at 10 – 300 K. The proton energy of 10 MeV is just enough to irradiate the whole sample-source sandwich with the samples still thick enough for the fast positron measurement.

As can be seen from Fig. 2.3, the cryostat and sample holder are movable and held in the "down" position during the irradiation, after which they are shifted about 15 cm upward for the positron measurement. In the first stage, positron

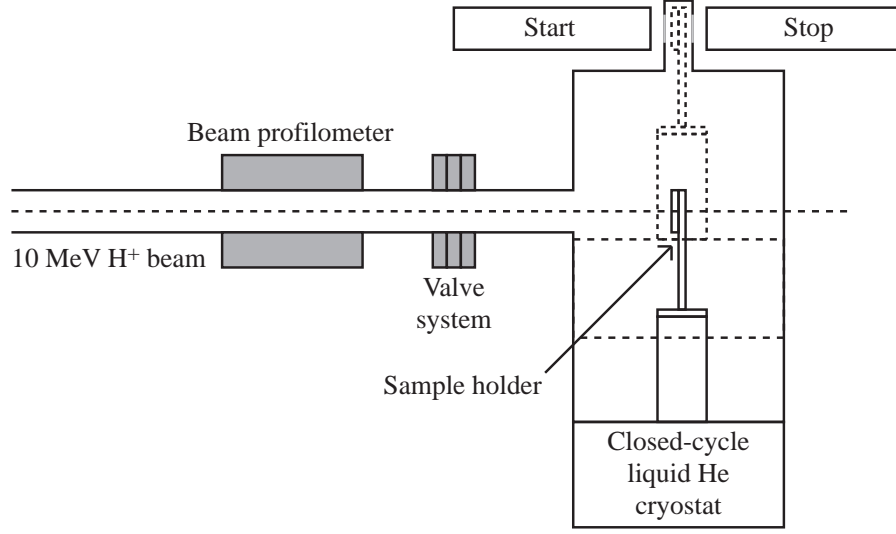


Figure 2.3: Schematic design of the low temperature positron measurement system connected to the 10 MeV proton beam line.

lifetime experiments are planned. The sample holder and the upper part of the measurement chamber are designed in a way that allows for the illumination of the sample-source sandwich during the positron measurements, enabling the study of optical ionization levels of the observed defects. The addition of a Ge detector to one side of the sample, or even a Doppler coincidence system, is possible.

The valve system connecting the positron measurement chamber to the proton beam line is such that the chamber can be disconnected (it has its own pumping system) from the rest of the facility while the sample is kept a 10 K. Hence the chamber can be moved to another location for the duration of the measurements that can take several months, if both illumination and annealing behavior are investigated, leaving the beam line free for other purposes. Another advantage of the disconnection possibility of the chamber is that a slow positron beam can be constructed separately and the chamber connected to it after irradiation without heating the sample, thus enabling low temperature irradiation measurements also in materials where thick samples are difficult or impossible to produce.

The irradiation facility with the fast positron measurement system has been constructed and it is currently being tested. The construction of a slow positron beam in connection with the facility is planned.

Chapter 3

Wide bandgap semiconductors for optoelectronics

GaN and ZnO are of particular interest as materials for blue and UV light emitting diodes and lasers due to their large band gap (about 3.4 eV at 300 K). The two materials have many similarities: they crystallize in the hexagonal wurtzite structure, and their lattice constants differ by only 2.3 %. However, the chemical difference of oxygen and nitrogen makes many properties of the two seemingly similar materials different. GaN is much more thermally stable than ZnO, which on the other hand makes the growth of bulk ZnO crystals clearly easier.

The advantage of GaN is that both *p*- and *n*-type doping are nowadays quite well understood. Hence GaN-based blue LEDs and lasers are commercially available. There are, however, still open questions, such as the details of the emission processes. The main disadvantage of GaN is the lack of native large-area substrates, and the heteroepitaxial layers typically suffer from a high dislocation density, detrimental to optical devices. The dislocation density typically decreases with layer thickness, and hence much effort is put into the research on how to produce thick quasi-bulk substrates. The method of choice is typically hydride vapor phase epitaxy due to the high growth rates achieved.

The main advantage of ZnO is the binding energy of the free exciton, about 60 meV, which is more than twice the corresponding value in GaN. In addition, native large-area substrates are readily available, the growth of ZnO can be performed at low temperatures, wet chemical etching is straightforward and electronic and optical properties are particularly resistant to particle radiation. The main problem is the lack of a reliable technology for producing *p*-type material. Interest in ZnO has increased very recently, 5 – 10 years later than in GaN, and hence many of the basic physical properties of the defects are still unknown.

3.1 Gallium nitride (GaN)

The properties of gallium nitride (GaN) depend strongly on the crystal orientation along the polar c -axis of the wurtzite structure. Studies on thin heteroepitaxial GaN overlayers grown on sapphire (Al_2O_3) by molecular beam epitaxy (MBE) [10,11] and metal-organic vapor phase epitaxy (MOVPE) [12] have shown that the layer polarity (Ga(0001) or N(000 $\bar{1}$)) has a significant impact on the incorporation of oxygen. However, the heteroepitaxial layers have a high dislocation density due to the substantial lattice mismatch between the layer and the substrate, which has been shown to affect the impurity incorporation, diffusion and point defect formation in the material [13]. Homoepitaxial growth of overlayers minimizes the impurity levels in the growth environment, since only native materials are present. No buffer layers are needed to produce different growth polarities, since the layers can be grown on different polarity surfaces of the substrate GaN crystal. Thus, layers with both polarities can be grown simultaneously.

The high pressure (HP) method [14,15] can be used to grow dislocation-free bulk GaN single crystals. Thick overlayers can be grown with hydride vapor phase epitaxy (HVPE) within reasonably short times. This provides an ideal system for investigating the effect of the growth polarity on the impurity incorporation and point defect formation. In addition to the low oxygen content of the substrate bulk GaN (compared to Al_2O_3), the lack of dislocations minimizes the diffusion of impurities from the substrate. Thus the properties of the HVPE layers should be independent of the layer thickness, in contrast to heteroepitaxial HVPE GaN, where the physical properties of the layers vary along the c -axis due to the dislocations [16]. The incorporation of impurities and formation of point defects during growth should then be limited by the (polarity dependent) surface kinetics and thermodynamics (independent of the polarity).

3.1.1 Polarity dependence of optical properties

In Publ. I we have studied the dependence on polarity of the optical properties of GaN layers grown by HVPE on HP grown GaN bulk crystals. The layers were grown to thicknesses 30–160 μm on specially prepared N and Ga polarity surfaces of bulk GaN substrates. The achieved growth rates were 15 – 80 $\mu\text{m}/\text{h}$. Details of the growth procedure can be found in Ref. [17]. The high crystallographic quality of the substrates, i.e. a density of dislocations as low as 10^2 cm^{-2} , is reproduced in the layers of both Ga and N polarities [18]. The optical properties of the layers were measured with infrared reflectivity (IR), μ -Raman scattering and photoluminescence (PL) spectroscopies.

The difference in the optical properties of between the N and Ga polar HVPE GaN

layers is seen in Fig. 3.1. The PL spectrum of the N polar layer is qualitatively very similar to the typical spectrum of HP GaN, exhibiting a yellow luminescence (YL) band. The Ga polar layer on the other hand shows excellent optical quality: the spectrum is dominated by exciton (X) and donor-acceptor pair (DAP) transition peaks and their satellites, with an intensity ratio (X/DAP) $\sim 10^3$. No YL is observed in the Ga polar layer.

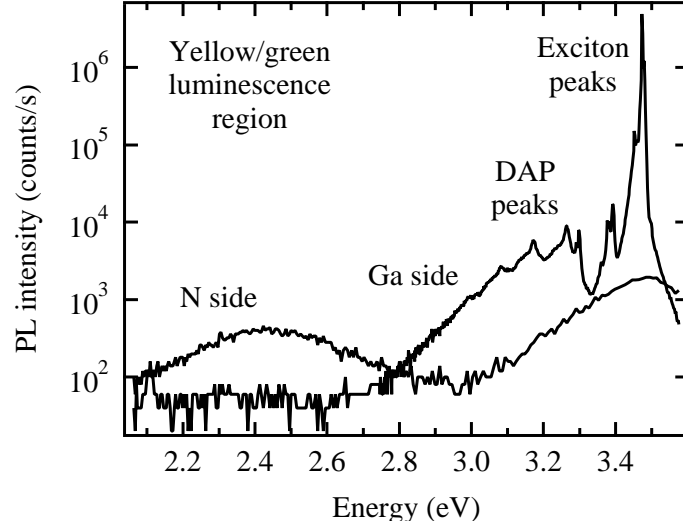


Figure 3.1: Photoluminescence spectra of the Ga and N polar HVPE GaN layers.

The difference between the N and Ga polar layers is clear also in IR and Raman scattering data. The IR spectrum of the N polar layer is dominated by the reflection from the free electron plasma, indicating a high free electron concentration N_e . By fitting the theoretical reflectivity to the data gives $N_e \simeq 7 \times 10^{19} \text{ cm}^{-3}$ for the N polar layer. The IR spectrum of the Ga polar layer on the other hand shows that the free electron concentration is below 10^{17} cm^{-3} . The μ -Raman spectra recorded in the layers are identical along the c -axis, showing the homogeneity of the layers. The LPP^+ mode frequency coincides with the $A_1(\text{LO})$ mode frequency in the Ga polar layer, indicating a low free electron concentration, while the spectrum measured on N polar side is similar to that in HP grown bulk GaN, where the free electron concentration is high.

The optical properties suggest that a high ($\sim 10^{19} \text{ cm}^{-3}$) concentration of donors (likely oxygen) is present in the N polar layers and is responsible for the high free electron concentration. The observation of the DAP and exciton peaks in the photoluminescence spectrum of the Ga polar layer is a clear indication of a low free electron concentration and supports the IR and μ -Raman results.

In summary, the material grown on the N polar side of GaN single crystals has a

high crystallographic quality but reproduces also the rather poor optical properties of the bulk GaN substrate. On the other hand, the layers grown on the Ga polar side combine the structural quality of the bulk crystal with excellent optical properties.

3.1.2 Vacancy defect and impurity incorporation

The homoepitaxial HVPE GaN samples presented in the previous section were studied with secondary ion mass spectrometry (SIMS) and positron lifetime spectroscopy in Publ. II. The impurity concentrations in the Ga and N polar layers are presented in Table 3.1. They are in good agreement with the observations based on the optical properties, *i.e.* the oxygen concentration is in the 10^{19} cm^{-3} range on the N side, while the concentration of all measured impurities is low on the Ga side.

Table 3.1: The impurity and defect concentrations in the GaN samples. c_{ion} and c_{cl} are the negative ion and vacancy cluster concentrations observed with positrons, respectively.

Defect [cm ⁻³]	HVPE GaN		bulk GaN	
	Ga polar	N polar	Ga polar	N polar
[O]	4×10^{17}	2×10^{19}	$4 \times 10^{19}{}^a$	$8 \times 10^{19}{}^b$
[Mg]	4×10^{16}	2×10^{17}	$1 \times 10^{18}{}^a$	
[C]	5×10^{16}	2×10^{17}		
[V _{Ga}]	$\leq 10^{15}$	7×10^{17}	2×10^{17}	7×10^{17}
c_{ion}	$\leq 10^{15}$	5×10^{18}	3×10^{18}	3×10^{18}
c_{cl}	$\leq 10^{15}$	$0.5 - 15 \times 10^{16}$	$\leq 10^{15}$	$0.5 - 15 \times 10^{16}$

^a Taken from Ref. [19]

^b Estimated from Ref. [20]

The positron lifetime measured in the HVPE layers grown on the Ga side of the substrate crystal is constant over the whole temperature range and the same in all samples, $\tau_{\text{ave}} = 160 \text{ ps}$ (Fig. 3.2). The lifetime spectrum has only a single component and τ_{ave} coincides with the lifetime of positrons in defect-free GaN [19], $\tau_B = 160 \text{ ps}$. Thus, in the Ga polar HVPE layers, the concentration of vacancy-type defects is below the sensitivity range of the method, $1 \times 10^{15} \text{ cm}^{-3}$.

The average positron lifetime measured in the Ga side of HP GaN is identical to that determined in earlier studies [19, 21] and similar in shape to those measured in the N polar samples (Fig. 3.2). In these three samples, τ_{ave} is longer than τ_B , which indicates the presence of vacancy defects. A second (higher) lifetime

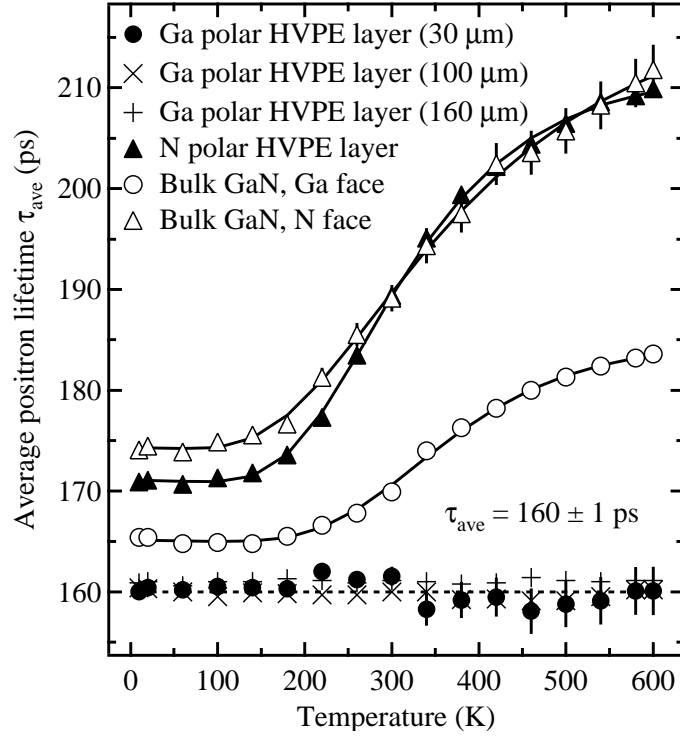


Figure 3.2: The average positron lifetime measured in the GaN samples. The solid lines represent the fits of the temperature dependent trapping model to the data.

component $\tau_2 = 235 \pm 10$ ps could be fitted to the experimental lifetime spectra measured in the Ga and N sides of HP GaN and in the N polar HVPE layer. This component can be attributed to the Ga vacancy, which is in the negative charge state and most likely complexed with oxygen [6, 21]. A third (higher) lifetime component $\tau_3 = 470 \pm 50$ ps could be fitted to the lifetime spectra measured in the two N polar samples. This component can be attributed to vacancy clusters which involve at least 20 vacancies. The decrease of the average positron lifetime with decreasing temperature in the samples where τ_{ave} is longer than τ_B is a clear indication of the presence of negative ion defects trapping positrons at low temperature to hydrogenic states where the positron lifetime is equal to τ_B [3, 19].

The concentrations of the Ga vacancies and negative ions can be estimated by fitting a temperature dependent trapping model [3, 19] to the lifetime data in Fig. 3.2. They are shown in Table 3.1. The negative ion concentration in the bulk crystals (Table 3.1) correlates with that of Mg, similarly as earlier [19]. The negative ion concentration in the N polar HVPE layer is significantly higher than the concentrations of Mg and C, indicating that other negative ion type defects

such as antisites or interstitials are also present in the layer.

As shown in Fig. 3.2a, the $V_{\text{Ga}} - \text{O}_{\text{N}}$ concentration is below the detection limit in the Ga polar HVPE layers of different thicknesses. On the other hand, the oxygen concentration in these homoepitaxial layers is higher than in the thickest heteroepitaxial layers studied in Refs. [6,16]. In spite of the lower oxygen content, Ga vacancies are observed in the latter [6]. This can be explained by the higher concentration of acceptor-type impurities such as Mg and C in the homoepitaxial layers, due to which the material is semi-insulating. The heteroepitaxial HVPE layers studied in Refs. [6,16] are n -type, and hence the formation energy of V_{Ga} is significantly lower.

The concentration of the vacancy clusters can be estimated to be $c_{\text{cl}} = 0.5 - 15 \times 10^{16} \text{ cm}^{-3}$. These vacancy clusters are likely to be the hollow pyramidal defects observed in Mg-doped GaN by TEM [22,23]. Similar clusters have been observed in Mg-doped MOCVD GaN also by positron annihilation spectroscopy [24]. All of these studies indicate that the clusters are correlated with high O and Mg impurity concentrations. From Table 3.1 it can be seen that the incorporation of both acceptor and donor type impurities is enhanced in the N polar growth of HVPE GaN, and the oxygen concentration is higher on the N side of HP GaN. These clusters can thus be formed by lateral overgrowth of the impurities [25], which would be natural due to the non-polar growth modes on the N polar surface.

The difference in the Ga vacancy concentrations between the Ga and N faces of HP GaN is significant. It correlates with the observation of a free carrier and oxygen concentration gradient along the c -axis [20]. As a compensating acceptor, the V_{Ga} concentration generally follows the increase of n -type doping [26]. The model in Ref. [20] proposes that the oxygen incorporation is much stronger during growth in the non-polar $(10\bar{1}0)$ directions, in which the N polar growth mainly proceeds. The Ga-polar growth on the other hand proceeds in the Ga polar (0001) direction. Recent experiments performed on non-polar HVPE GaN grown on R-plane sapphire [27] also support this model. The model provides an explanation also for the difference in the Ga vacancy and oxygen concentrations between the Ga and N polar homoepitaxial HVPE GaN layers, where the difference between the polarities is larger than in the bulk GaN crystals. The temperature and pressure are lower in HVPE growth, which reduces the oxygen diffusion, and there is more oxygen present in the high-pressure growth.

It is worth noticing that the Ga vacancy and O impurity concentrations ($[V_{\text{Ga}}] \simeq 7 \times 10^{17} \text{ cm}^{-3}$, $[\text{O}] \simeq 2 \times 10^{19} \text{ cm}^{-3}$) are the same in the N polar HVPE layer and N polar side of the substrate bulk GaN, although their growth temperatures were very different (around 1300 K in the HVPE and 1800 K in the HP growth). The isolated Ga vacancies become unstable at temperatures 500 – 600 K [28], thus the Ga vacancies observed in the HVPE and bulk GaN samples are likely

complexed with oxygen. Considering the calculated formation energies [26] of V_{Ga} and $V_{\text{Ga}} - \text{O}_{\text{N}}$ ($E_V^f \simeq 1.3$ eV and $E_{VO}^f \simeq 1.0$ eV in n -type GaN) as well as the available sites of formation (limited by the oxygen concentration for the latter), the equilibrium concentrations of isolated Ga vacancies at the growth temperatures dominate by a factor of roughly 100, in spite of the lower formation energy of the complex. Thus, the final concentration of $V_{\text{Ga}} - \text{O}_{\text{N}}$ in the material is determined by the ability of the isolated vacancies to diffuse and form pairs with the oxygen impurities. However, the $V_{\text{Ga}} - \text{O}_{\text{N}}$ complexes have been observed to be unstable above 1300 K [28]. Thus the $V_{\text{Ga}} - \text{O}_{\text{N}}$ concentrations are determined by the equilibrium at about 1300 K during cooling down, resulting in $[V_{\text{Ga}}] \simeq 10^{17} - 10^{18} \text{ cm}^{-3}$ in both materials.

3.2 Zinc Oxide (ZnO)

Good-quality ZnO single crystals have been available for a relatively short period of time, and hence many basic defect properties are still unknown. Point defects can be introduced in concentrations much larger than those given by the thermodynamic equilibrium during growth and cooling down by means of irradiation of the material *e.g.* by electrons. The study of the formation of point defects under these non-equilibrium conditions gives information on the basic physical properties of the semiconductor material. Electron paramagnetic resonance (EPR) studies of electron and neutron irradiated ZnO [29–36] have shown that interstitial and vacancy defects are produced at low temperatures on both sublattices.

The photoluminescence spectrum of ZnO typically exhibits a green luminescence (GL) band similar to the yellow luminescence in GaN [37]. Both the Zn [37,38] and O [39–41] vacancies have been proposed to be the defect responsible for this GL band. However, the conclusive identification is still lacking. Both the optical and electrical properties of ZnO are much more resistant than those of GaN to deterioration caused by room temperature electron and proton irradiation [42,43], which makes it potentially useful for applications in high-irradiation environments. The microscopic origin of the radiation hardness of ZnO is not, however, well understood.

Similarly as in other semiconductor materials, the choice of substrate material and orientation affects the properties of overgrown thin layers. As in the case of GaN, sapphire is a potential substrate for mass production of thin ZnO films due to relatively low cost and transparency up to about 6 μm wavelength. However, the heteroepitaxy presents several problems due to differences in the chemical and physical properties of the two materials.

3.2.1 Identification of vacancy defects

We have used positron annihilation spectroscopy to identify and quantify the open volume defects in both as-grown (Publ. III) and electron irradiated (Publ. III and IV) ZnO single crystals. The nominally undoped samples were grown by the seeded vapor phase technique [44]. For the study of irradiation-induced defects, two samples were irradiated with 2 MeV electrons with fluence $6 \times 10^{17} \text{ cm}^{-2}$. The acceptor densities in the samples were determined by temperature dependent Hall measurements [45], where the mobility data is analyzed by fitting to it the solution of the Boltzmann transport equation [44]. The Fermi levels are 0.1 eV and 0.2 eV below the conduction band in the as-grown and irradiated samples, respectively.

The results of the positron lifetime measurements in both the as-grown and irradiated ZnO samples are presented as a function of measurement temperature in Fig. 3.3. At 300 – 500 K the average positron lifetime in the as-grown sample is constant or very slightly increasing due to the thermal expansion of the lattice. It provides the lifetime of the positron in the delocalized state in the ZnO lattice, $\tau_B = 170 \text{ ps}$ at 300 K. The increase in the average positron lifetime with decreasing temperature at 10 – 300 K is a clear indication of the presence of negatively charged vacancies, the positron trapping coefficient of which increases with decreasing temperature. The lifetime spectrum could be decomposed into two lifetime components at 10 K, giving $\tau_2 = 265 \pm 25 \text{ ps}$ for the higher component. The large uncertainty in τ_2 is due to the fact that the increase in τ_{ave} is very small, only 3 ps, because of the small intensity I_2 .

The same increase in the average positron lifetime with decreasing temperature at 10 – 300 K is observed in the irradiated sample (Fig. 3.3). Here τ_{ave} is clearly above the bulk value τ_B and thus the decomposition of the lifetime spectra could be performed with much greater accuracy. The higher lifetime component τ_2 of the irradiated sample is presented in the upper part of Fig. 3.3, the average value is $\tau_2 = 230 \pm 10 \text{ ps}$, within experimental accuracy the same as $\tau_2 = 265 \pm 25 \text{ ps}$. The characteristic S_D and W_D parameters of the vacancy defect could be determined from the irradiated sample data by fitting the equation for the fraction of annihilations at defects (Eq. (2.7)) to the $W(S)$ data. The scaled S and W parameters of the defect were obtained as $S_D/S_B = 1.039(4)$ and $W_D/W_B = 0.87(3)$. The S and W parameters of the bulk lattice were determined from the as-grown sample in the temperature region 300 – 500 K.

Figure 3.4 presents the momentum distribution measured with the conventional coincidence Doppler setup in the as-grown sample at 300 K, representing the bulk distribution, and two defect-specific distributions separated from the spectra measured at 10 K and 150 K from the irradiated sample. In the case of the as-grown sample, the defect-specific momentum distribution could not be separated due

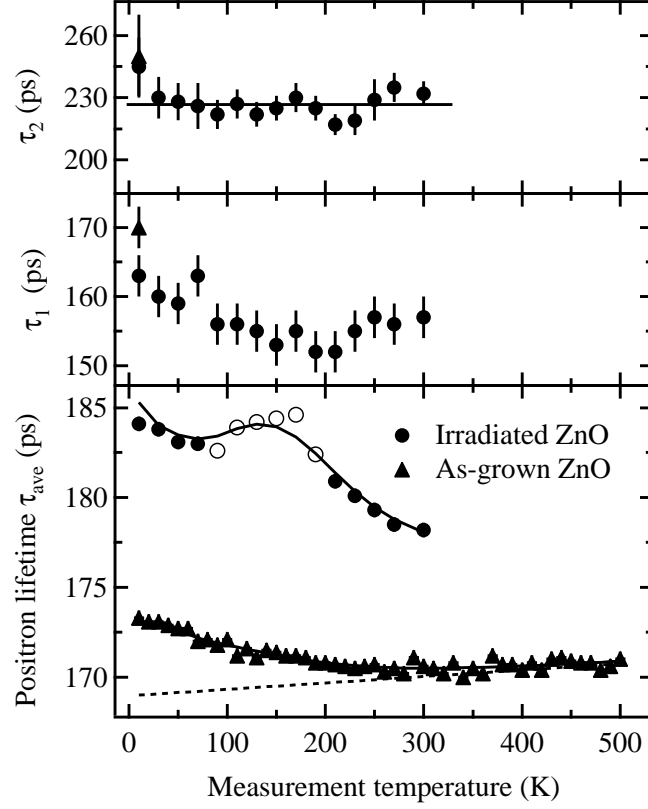


Figure 3.3: The positron lifetime and Doppler broadening parameters of the as-grown and irradiated samples plotted as a function of measurement temperature. The data markers are drawn as open in the temperature range 90 – 190 K, where the effect of the O vacancies is the most visible.

to the low intensity of the second lifetime. We calculated the positron lifetimes and core electron momentum distributions by solving the positron state and constructing the electron density of the wave function of the free atoms, similarly as described in Ref. [46]. The calculated momentum distributions for the bulk state, the oxygen vacancy (V_O) and the zinc vacancy (V_{Zn}) are presented in the upper part of Fig. 3.4. The results show clearly that the core electron momentum distribution at V_O is indistinguishable from the distribution in the perfect lattice. On the other hand, the effect of the defect in the measured spectra is the same as the one of V_{Zn} in the calculated spectra, thus the defect can be identified as V_{Zn} . Further support for the identification of the Zn vacancy is obtained from the experimental values of τ_D/τ_B , S_D/S_B , and W_D/W_B , which are similar to the corresponding values of the Ga vacancy in GaN [21,24]. In addition, 2 MeV

electron irradiation with similar fluence as in this work is known to produce Ga vacancies in GaN [28].

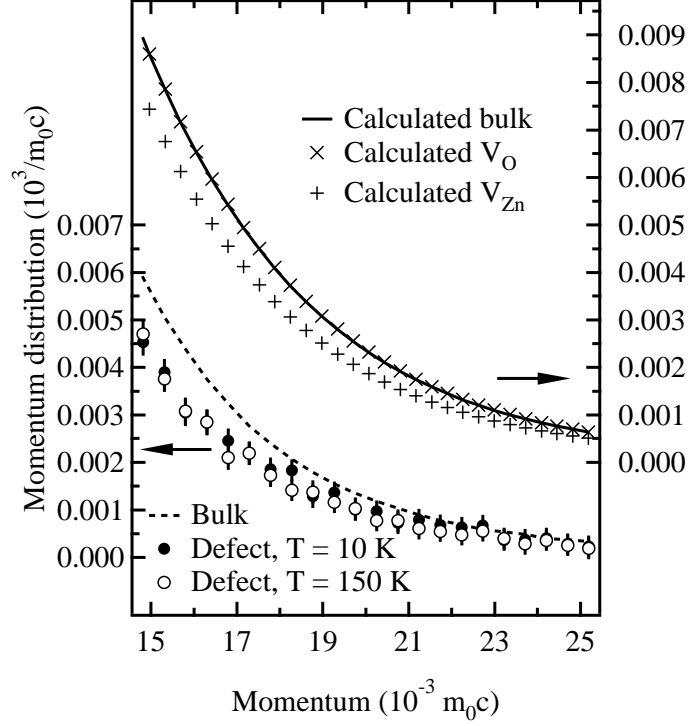


Figure 3.4: The measured and calculated core electron momentum distributions in ZnO.

The Doppler broadening parameters S and W fall on a line when plotted against each other with temperature as the running parameter, which typically indicates the presence of only two distinguishable positron states (bulk and vacancy). The negative ion type defects do not cause deviations from the straight line, since the annihilation parameters of positrons trapped at these shallow traps coincide with the bulk parameters. However, as can be seen in Fig. 3.5, the points measured at 90 – 190 K in the irradiated samples fall off the straight line determined by the annihilations in the bulk lattice and the Zn vacancy. This implies that a third positron state can be distinguished in the lifetime vs. Doppler parameter data although the Doppler data itself is linear. In order to cause a deviation from the straight line, the localization to this defect needs to be strong, implying that the defect has a distinguishable open volume. The open volume of this defect cannot be very large, since the independence of temperature of the higher lifetime component τ_2 shows no evidence of the mixing of several lifetime components. Hence, the lifetime specific to this defect needs to be sufficiently far from τ_2

(and closer to τ_1), below 200 ps. In addition, in order to produce the deviation observed in Fig. 3.5, the defect-specific lifetime needs to be above τ_{ave} over the whole temperature range, *i.e.* above 185 ps.

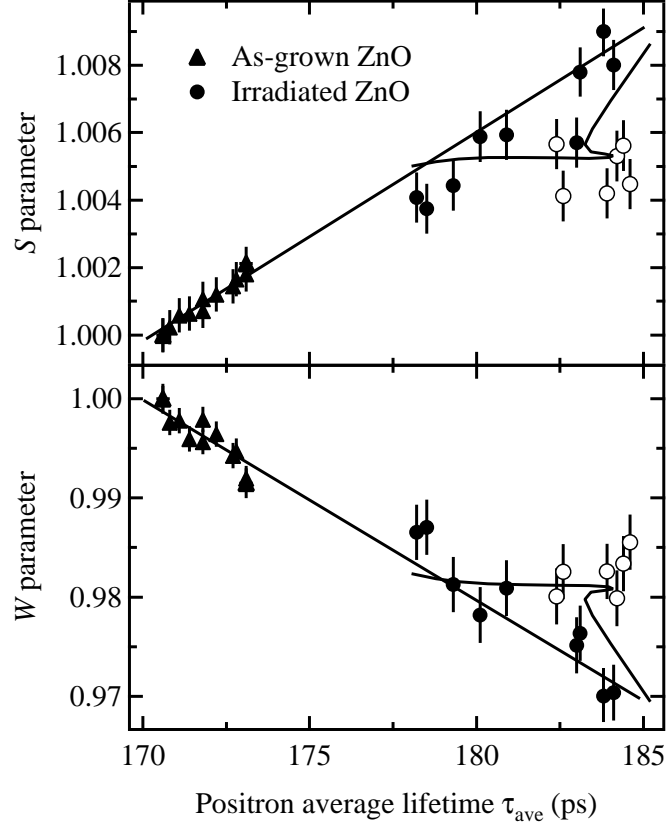


Figure 3.5: The S and W parameters plotted as a function of τ_{ave} . The data markers are drawn as open in the temperature range 90 – 190 K, where the effect of the O vacancies is the most visible.

One additional aspect of the third type of defects is evident from the τ_{ave} vs. T data. The fraction of positrons annihilating as trapped at this defect is vanishing at room temperature and clearly smaller than the annihilation fractions to the Zn vacancies and negative ion type defects below 90 K, but larger at the intermediate temperature 90 – 190 K. This implies that enhancement of positron trapping with decreasing temperature is larger in this defect at temperatures 190 – 300 K, but saturates around 150 K, where the Zn vacancies and negative ion type defects become more important. This indicates that the third type of defect is neutral, and the temperature dependence of the positron trapping observed at high temperatures is due to either thermal escape from the defect or a change in the charge

state of the defect. Based on these considerations and especially the lifetime value of 190 – 200 ps, a prominent candidate for this defect is the O vacancy, which has a donor nature and would naturally have a smaller open volume than the Zn vacancy.

The temperature dependent trapping model can be used to estimate the trapping rates to the different defects from the τ_{ave} vs. T data in Fig. 3.3 using the defect specific positron lifetimes $\tau_{V,\text{Zn}} = 230$ ps, $\tau_{V,\text{O}} = 195$ ps and $\tau_{\text{st}} = 170$ ps for the Zn vacancies, O vacancies and negative ion type defects, respectively. Assuming that the temperature dependence of the trapping to the O vacancies is due to the thermal escape of positrons at high temperatures does not fit well to the data, since the changes in the trapping rate are not steep enough to reproduce the experimentally observed temperature dependent behavior. Hence the ionization of the neutral O vacancy is the source of the temperature dependence of its trapping rate. The fitted trapping rates are shown in the lower panel of Fig. 3.6. The origin of temperature dependent behavior of the positron data can be seen from the figure. The trapping rate to the Zn vacancies increases as $T^{-0.5}$ with decreasing temperature, while the thermal detrapping causes the trapping rate to the negative ions to vanish above 150 K. The trapping rates to the two negative defects coincide at temperatures below 70 K.

The trapping rate to the O vacancies is negligible at 300 K, but increases rapidly with decreasing temperature. At temperatures 100 – 200 K, it is significantly higher than the sum of the trapping rates to the Zn vacancies and the negative ion type defects, causing the deviation from the one vacancy type defect model (straight line) in Fig. 3.5. Below 100 K, the trapping rate to the negative defects increases very rapidly and the trapping rate to the O vacancies has saturated to a constant value (all the O vacancies are neutral), making the effect of the O vacancies on the positron data small. The effect is observed as a maximum in the annihilation fraction of the O vacancies at around 130 K (upper panel of Fig. 3.6).

The concentrations of the defects in the irradiated material can be estimated from the trapping rates in a straightforward matter. Assuming a trapping coefficient of $\mu_{V,\text{Zn}} = 3 \times 10^{15} \text{ s}^{-1}$ at 300 K for the Zn vacancy as for the Ga vacancy in GaN [28] we obtain $[V_{\text{Zn}}] \simeq 2 \times 10^{16} \text{ cm}^{-3}$. At 30 K $\kappa_{\text{st}} \simeq \kappa_{V,\text{Zn}}$, and assuming that the trapping coefficient of the negative ion type defect is similar to that of a negative vacancy [3, 47], the concentrations are also similar, $c_{\text{st}} \simeq 2 \times 10^{16} \text{ cm}^{-3}$. The trapping coefficient of a neutral vacancy is lower than that of a negative vacancy [48], and taking a value of $\mu_{V,\text{O}} = 1 \times 10^{15} \text{ s}^{-1}$ for the neutral O vacancy results in a concentration of $[V_{\text{O}}] \simeq 3 \times 10^{17} \text{ cm}^{-3}$. In the as-grown material, where the Zn vacancies are the only defect observed by positrons, their concentration is estimated as $[V_{\text{Zn}}] \simeq 2 \times 10^{15} \text{ cm}^{-3}$.

The only negative defect observed by positrons in the as-grown ZnO sample is the

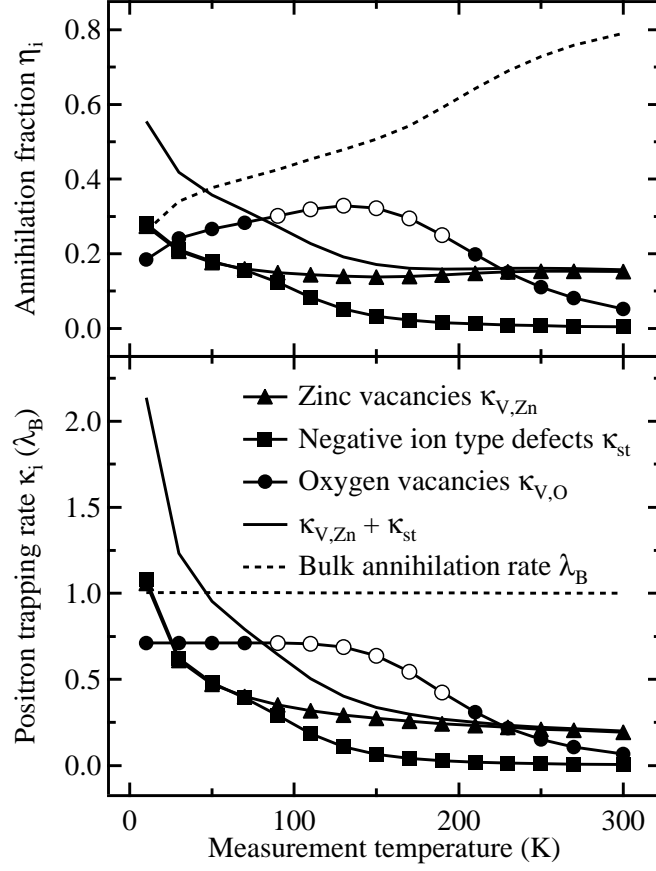


Figure 3.6: The positron trapping rates and corresponding annihilation fractions of the different defects as a function of temperature. The data markers are drawn as open in the temperature range 90 – 190 K, where the effect of the O vacancies is the most visible.

Zn vacancy, thus indicating that it is the dominant intrinsic acceptor in n -type ZnO. According to calculations in Ref. [38], the doubly negatively charged state of the zinc vacancy (V_{Zn}^{2-}) has the lowest formation energy when the Fermi level is near the bottom of the conduction band. Thus the Zn vacancies in the studied samples are mostly in this state.

The introduction rate of a defect D can be estimated as $\Sigma_D = [D]/\Phi$, where $\Phi = 6 \times 10^{17} \text{ cm}^{-2}$ is the irradiation fluence. With the defect concentrations $[V_{\text{Zn}}] \simeq c_{\text{st}} \simeq 2 \times 10^{16} \text{ cm}^{-3}$ and $[V_{\text{O}}] \simeq 3 \times 10^{17} \text{ cm}^{-3}$, the corresponding introduction rates are obtained as $\Sigma_{V_{\text{Zn}}} \simeq \Sigma_{\text{st}} \simeq 0.03 \text{ cm}^{-1}$ and $\Sigma_{V_{\text{O}}} \simeq 0.5 \text{ cm}^{-1}$. The introduction rate of the Zn vacancies is about 30 times lower than determined for

Ga vacancies in GaN [28], manifesting the radiation hardness of ZnO. In addition, as the introduction rates of primary defects are typically $\simeq 1 \text{ cm}^{-1}$, both the Zn vacancies and negative ions are probably formed through recombination processes during the irradiation and are thus parts of defect complexes. This is supported by the observations that the isolated Zn vacancies [30] and probably isolated interstitials on both sublattices [29] are mobile well below room temperature. On the other hand, the introduction rate of the O vacancies suggests that *they* are primary defects, and comparison to results obtained from EPR measurements [35, 36], which show that the isolated O vacancy is stable at room temperature, suggests that the O vacancies observed in this work are isolated.

We studied the optical activity of the in-grown and irradiation-induced defects by shining monochromatic light on the samples during the positron experiments at 20 K. The results are presented in Fig. 3.7. No effect is observed in the as-grown ZnO samples, where the average positron lifetime remains constant when the photon energy is varied between 0.7 and 3.1 eV. On the other hand, in the irradiated material, a small increase of the average positron lifetime is visible when the photon energy is increased to 2.3 eV, followed by a decrease to the value in the dark with further increase of the photon energy.

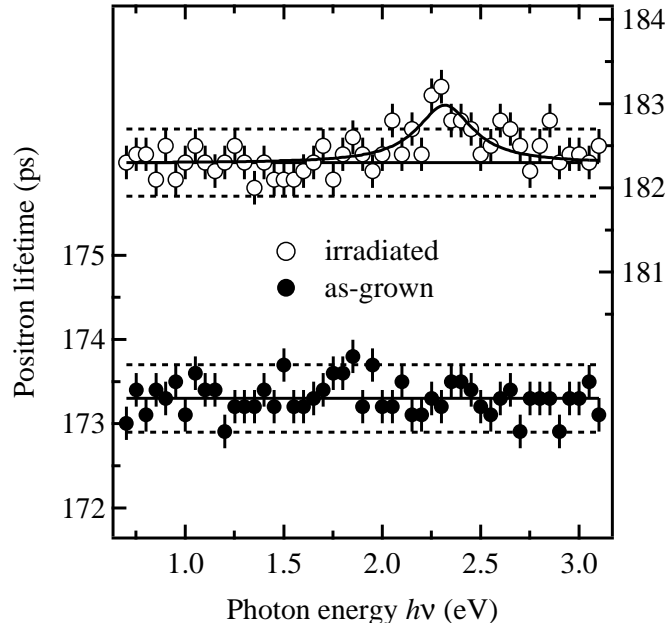


Figure 3.7: The average positron lifetime measured at 20 K in the as-grown and irradiated ZnO samples as a function of illumination photon energy.

The behavior of the average positron lifetime under illumination at low temperature in Fig. 3.7 can be explained in the following way. As seen from Fig. 3.6, the

positron data is dominated by the Zn vacancies and negative ion type defects at the measurement temperature of 20 K. Thus it is natural to assign the observed optical activity to these defects. The Zn vacancies are mostly in the doubly negative charge state (and cannot become more negative), and hence the increase of the average positron lifetime when approaching the illumination photon energy of 2.3 eV from below indicates that the negative ion type defects become less negative or even neutral and start trapping positrons less efficiently, increasing the fraction of positron annihilations at the Zn vacancies. The subsequent decrease of the positron lifetime with the further increase of the illumination photon energy then indicates that the Zn vacancies become less negative in their turn. This can be interpreted as both the Zn vacancies and the negative ions having an ionization level close to 2.3 eV. According to theoretical calculations [38], the $V_{\text{Zn}}^{2-/-}$ transition should occur at $E_C - 2.6$ eV, in good agreement with our data. The same work predicts that the O interstitial (octahedral position) has the $O_I^{2-/-}$ transition at $E_C - 2.4$ eV, and the O antisite has the $O_{\text{Zn}}^{2-/0}$ transition at $E_C - 2.3$ eV. This supports the tentative identification of the negative ion as the O_I or O_{Zn} .

3.2.2 Stability of intrinsic defects

The thermal recovery of point defects introduced by electron irradiation in ZnO was studied in Publ. IV. Both the as-grown and irradiated ZnO samples were *in situ* thermally annealed in the positron measurement cryostat for 30 min. at temperatures up to 600 K. No changes in the positron parameters were observed in as-grown ZnO. The average positron lifetime measured at four different temperatures in the irradiated samples is presented as a function of annealing temperature in Fig. 3.8. The positron lifetime decreases with increasing annealing temperature and reaches the level of the as-grown material at the annealing temperature of 590 K, above which no further changes were observed. The higher lifetime component $\tau_2 = 230 \pm 10$ ps is also shown in Fig. 3.8. The experimental spectra are two-componential up to the highest annealing temperatures, where the separation could be performed only at low measurement temperatures due to the small concentration of the defects. In addition, the second lifetime component τ_2 , specific to the Zn vacancy, remains constant throughout the whole annealing temperature range, implying that it truly represents positrons annihilating in one bound state rather than a superposition of several bound states.

The trapping rates to the Zn vacancies, negative ion type defects and O vacancies can be directly estimated from the positron data without fitting. They are presented in Fig. 3.9. It is clearly seen that the interpretation of the results presented above is correct: the Zn vacancies anneal out of the material at two separate stages at around 400 K and 550 K, the negative ion type defects anneal

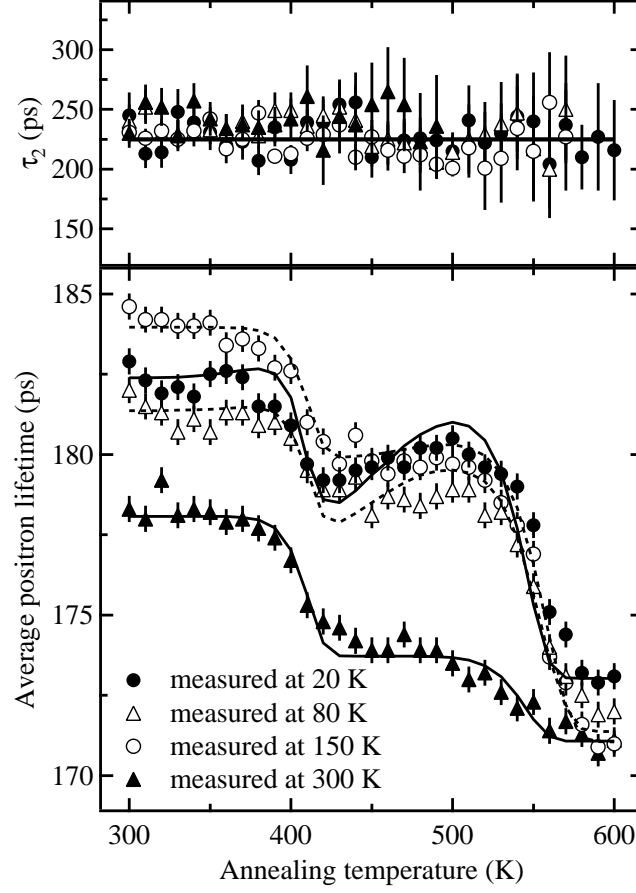


Figure 3.8: The average positron lifetime in the irradiated ZnO sample as a function of the annealing temperature. The higher lifetime component is shown in the upper panel.

out around 450 K and the O vacancies anneal out together with the second part of the Zn vacancies above 550 K. The temperature at which the O vacancies recover is in good agreement with a recent EPR study [36], where the O vacancies are observed to disappear between 570 K and 670 K.

The trapping rates are directly proportional to the defect concentrations, and thus the trapping rates and activation energies E_A corresponding to different annealing stages can be fitted to the data in Fig. 3.9. Three annealing stages of the point defects produced by electron irradiation in *n*-type ZnO are observed in the temperature range 300–600 K. The first annealing stage occurs at about 400 K and consists of the recovery of 40 % of the irradiation-induced Zn vacancies, with an activation energy of $E_{A1}^{V_{\text{Zn}}} = 1.3 \pm 0.1$ eV. The second annealing stage covers

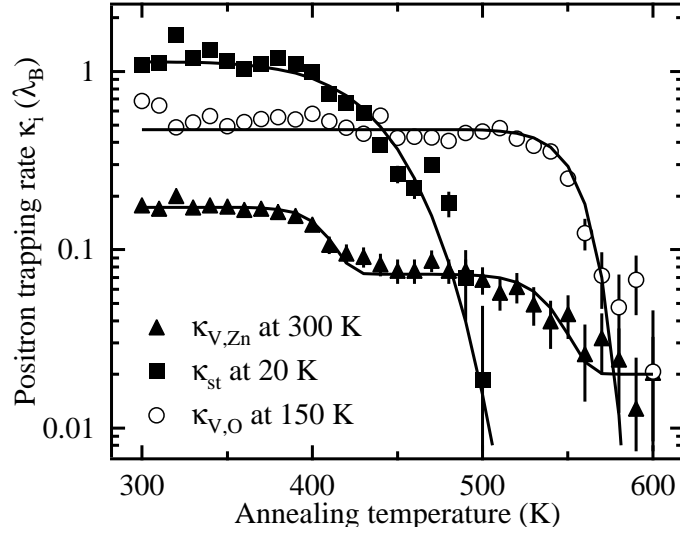


Figure 3.9: The positron trapping rates to the different defects as a function of the annealing temperature.

the temperature range 400 – 500 K, where the negative ion type defects recover, with activation energies ranging from 1.4 ± 0.1 eV at the beginning of the anneal at about 400 K to 1.6 ± 0.1 eV at the end at about 500 K. The third annealing stage occurs at about 550 K and consists of the recovery of the O vacancies and of the remaining irradiation-induced Zn vacancies, with an activation energy of $E_{A2}^{V,Zn} \simeq E_A^{V,O} = 1.8 \pm 0.1$ eV. The positron data shows that the irradiation-induced defects have fully recovered after this final annealing stage, in perfect agreement with the results of electrical measurements [42].

The observation of two separate annealing stages of the Zn vacancies indicates that two different defect complexes are involved in their recovery. This can be interpreted as the formation of two different Zn vacancy related complexes in the irradiation, of which one would be more stable than the other and anneal at the later stage. The first annealing stage could also be interpreted as the filling of a part of the Zn vacancies by interstitials released from other irradiation-induced defect complexes, not observed by positrons.

3.2.3 Vacancies in thin heteroepitaxial layers

The effect of the substrate orientation and layer thickness on the point defect distribution in thin heteroepitaxial ZnO layers was studied in Publ. V. The layers were grown by metal-organic chemical vapor deposition (MOCVD) at a temperature of 690 K to thicknesses 500–2000 nm on sapphire substrates with orientations

$(1, 1, -2, 0)$, $(0, 0, 0, 1)$, $(1, 0, -1, 0)$ and $(1, -1, 0, 2)$, corresponding to a , c , m and r planes, respectively. The positron experiments were carried out at room temperature with a slow positron beam in the 0 – 40 keV range. The layer-specific Doppler parameters were determined at energies 5 – 15 keV.

The layer-specific S and W parameters are presented in Fig. 3.10 as relative to the values in the bulk ZnO single crystal studied in more detail in Publ. III. Only annihilations from the free (diffusive) state in the lattice are observed in this sample at room temperature. Figure 3.10 shows also the point of saturation trapping at Zn vacancies, estimated from the data obtained in the electron irradiated ZnO samples in Publ. III. All the measured layer parameters fall on the line between the bulk (1,1) point and the Zn vacancy specific point, indicating that the Zn vacancy is the dominant open volume defect trapping positrons in the layers.

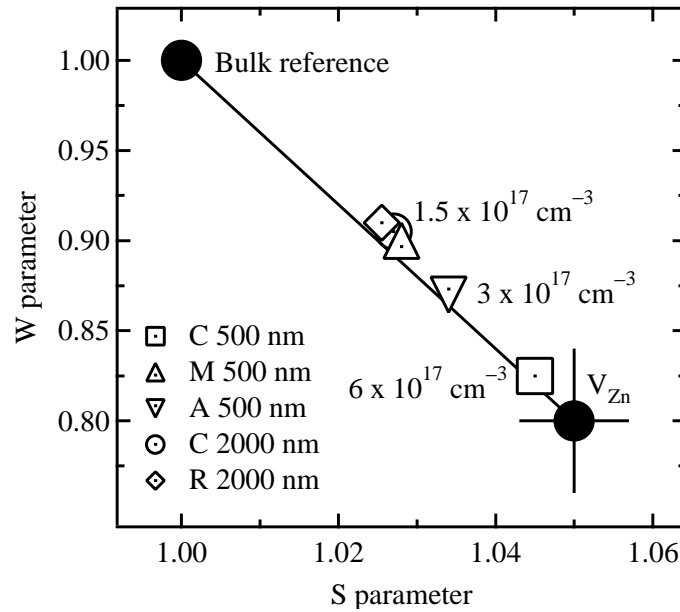


Figure 3.10: W/S plot of the layer-specific Doppler parameters in all the studied ZnO layers.

The Zn vacancy concentrations (also shown in Fig. 3.10) are obtained from the kinetic trapping model, assuming a trapping coefficient of $3 \times 10^{15} \text{ s}^{-1}$ at room temperature. As can be seen in the figure, the Zn vacancy concentration depends on the plane of sapphire over which the layer has been grown. In the 500 nm thick layers the concentration is clearly lowest in the layer grown over the m -plane sapphire orientation, where scanning force microscopy shows flat surfaces [49]. The a and c planes of sapphire present well-defined stepped surfaces that produce a different morphology. This different morphology seems to be significant to the

Zn vacancy concentration, even for samples 500 nm thick. This could be evidence of a different internal microstructure of grains even at long distances from the interface.

The Zn vacancy concentration of the ZnO layer grown over the *c*-plane of sapphire decreases about four times when increasing the film thickness from 500 nm to 2000 nm. It is interesting to notice that in the case of ZnO grown over *r*-plane sapphire, the concentration of Zn vacancies is very close to the one found in the thick ZnO layer grown over the *c*-plane of sapphire. The dependence on film thickness is similar to the one found in the heteroepitaxy of GaN [6], where it can be associated with increased doping due to oxygen diffusion from the substrate. However, in ZnO oxygen diffusion from sapphire should not have such a role. Therefore, the presented results indicate that the largest vacancy concentration induced in the layer occurs at the first steps of the growth, probably caused by the misorientation of the substrate planes.

Chapter 4

Magnetically doped semiconductors for spin electronics

Semiconductor spin electronics (or spintronics for short) aims at developing material systems in which novel mechanisms of control over magnetization in magnetic compounds or over individual spins in semiconductor nanostructures could lead to new functionalities in classical and quantum information hardware, respectively. Today's spintronics research involves virtually all materials families. However, ferromagnetic semiconductors, which combine complementary functionalities of ferromagnetic and semiconductor material systems, appear to be particularly interesting. For instance, it can be expected that powerful methods developed to control the carrier concentration and spin polarization in semiconductor quantum structures could serve to tailor the magnitude and orientation of magnetization produced by the spins localized on magnetic ions.

The possibility to include magnetic impurities such as manganese (Mn) at high concentrations in GaAs offers good prospects of combining magnetic phenomena with high speed electronics and optoelectronics [50, 51]. The ferromagnetic coupling in (Ga,Mn)As is mediated by holes [52]. Important magnetic properties, such as the Curie temperature and the saturation magnetization, have been shown to be directly related to the concentration of the holes [52–54]. Thus, the compensation of the holes is an important topic to study. In-grown point defects act as compensating centers and thus have a strong effect on the magnetic properties. The concentrations of these native defects depend on their thermodynamical formation energies. However, in GaAs grown at low temperature, the growth kinetics have an influence on the defect concentrations as demonstrated before in low temperature molecular beam epitaxy (LT-MBE) grown GaAs [55–60].

4.1 Gallium arsenide (GaAs) doped with Mn

In Publ. VI we investigated the thermodynamical and kinetic behavior of native point defects in LT-MBE $\text{Ga}_{1-x}\text{Mn}_x\text{As}$. The arsenic-rich growth stoichiometry produces defects mainly in the Ga sublattice of both donor (As antisite As_{Ga}) and acceptor (Ga vacancy) type. The $\text{Ga}_{1-x}\text{Mn}_x\text{As}$ layers were grown in a Kryovak LT-MBE system dedicated to III-Mn-V magnetic semiconductors on semi-insulating (SI) Freiberger GaAs wafers at temperatures 210–240 °C, see Ref. [61] for more details. The As_2 flow was kept low during growth in order to minimize the production of As antisites. The Mn concentration in the layers was varied between 0.5 and 5 % and the layer thicknesses were 0.5 – 1.5 μm . The hole concentrations in the as-grown layers determined by Hall measurements were about 30 % of the Mn concentrations. No post-growth annealings were performed.

The infrared absorption experiments were carried out in the transmission configuration. Three samples with $\text{Ga}_{1-x}\text{Mn}_x\text{As}$ layer thickness 1.5 μm and Mn content of 1, 3 and 5 % were measured. A sample cut from the substrate SI GaAs was used as a reference. The absorption coefficient μ_{layer} of the layer could be extracted from the knowledge of the corresponding value of the substrate, μ_{subst} , using the equation $\phi_{\text{out}}(h\nu) = \phi_{\text{in}}(h\nu) \exp(-(\mu_{\text{layer}}d_{\text{layer}} + \mu_{\text{subst}}d_{\text{subst}}))$. Here, ϕ_{out} and ϕ_{in} are the outgoing and ingoing light fluxes as functions of the photon energy $h\nu$, respectively, and the layer and substrate thicknesses are denoted by d . The measurements were carried out using a relatively high incoming light flux of $\phi_{\text{in}} \approx 10^{16} \text{cm}^{-2}\text{s}^{-1}$ so that the occupation of the electron states is dominated by the optical transitions. The positron annihilation studies were carried out at room temperature using a variable energy ($E = 0 - 40 \text{ keV}$) positron beam. The measured spectra were characterized by the conventional low momentum (S) and high momentum (W) lineshape parameters.

The absorption coefficient measured in the $\text{Ga}_{1-x}\text{Mn}_x\text{As}$ layers as a function of incoming photon energy has a step-like form around $h\nu = 1.15 \text{ eV}$, similar as measured many times before in Czochralski-grown SI bulk GaAs and attributed to the electron transitions from As_{Ga} defect level to the conduction and valence bands [62–65]. The absorption coefficient μ is determined by both the concentrations of the neutral and positive antisites and the absorption cross-sections of the electrons (σ_n) and holes (σ_p), respectively. Under illumination the concentrations are related through $[\text{As}_{\text{Ga}}^0] = [\text{As}_{\text{Ga}}^{\text{tot}}]\sigma_p/(\sigma_p + \sigma_n) = [\text{As}_{\text{Ga}}^+]\sigma_p/\sigma_n$ and the absorption coefficient can be written as

$$\mu = \sigma_n[\text{As}_{\text{Ga}}^0] + \sigma_p[\text{As}_{\text{Ga}}^+] = \frac{2\sigma_n\sigma_p}{\sigma_n + \sigma_p}[\text{As}_{\text{Ga}}^{\text{tot}}]. \quad (4.1)$$

The values of σ_n and σ_p around $h\nu = 1.15 \text{ eV}$ have been determined by many

authors [62–65], resulting in $\sigma_0 = 2\sigma_n\sigma_p/(\sigma_n + \sigma_p) = 0.7(3) \times 10^{-16} \text{ cm}^2$. The total concentrations of the As antisites are estimated to be about 10 % – 20 % of the Mn content. They are presented in Fig. 4.1 together with Ga vacancy concentrations.

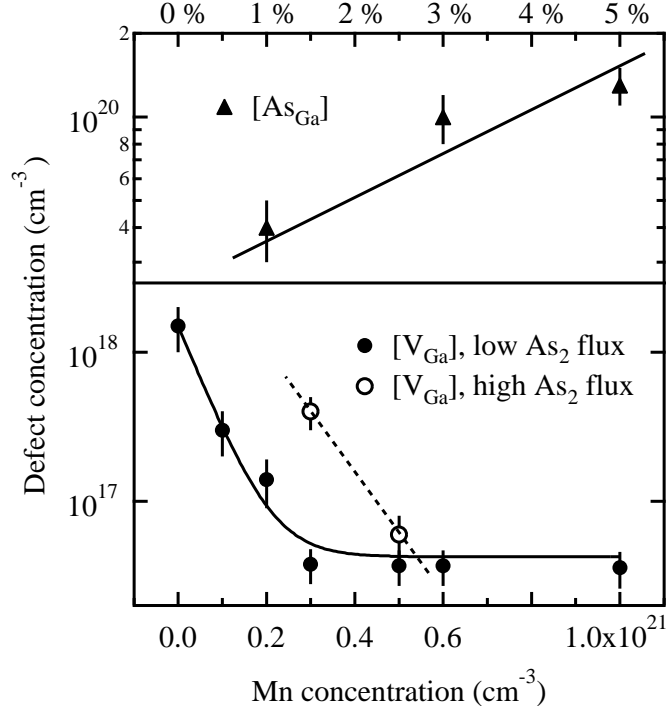


Figure 4.1: The Ga vacancy and As antisite concentrations in the $(\text{Ga},\text{Mn})\text{As}$ layers as a function of the Mn concentration.

The S and W parameters determined in the $\text{Ga}_{1-x}\text{Mn}_x\text{As}$ layers fall on the line connecting the specific parameters of defect-free GaAs [66] and the Ga vacancy [55, 58], giving evidence that the vacancy defect observed in the layers is the Ga vacancy. Further identification of the Ga vacancy is obtained from two-Ge-detector coincidence measurements of the Doppler broadening. The behavior of the high-momentum part of the positron-electron distribution is the same in both the LT GaAs and $\text{Ga}_{1-x}\text{Mn}_x\text{As}$ layers, and similar as observed in previous measurements in GaAs [67]. The core electron momentum distribution shows the typical signature of As 3d electrons [57, 67], indicating directly that the vacancy is in the Ga sublattice.

In order to determine the concentrations of the Ga vacancies, we measured the S and W parameters in the layers also as a function of measurement temperature in the range 100–370 K. The decrease of the S parameter due to positron trapping at

negative ion type defects was observed below room temperature in the layer with 0.5 % of Mn, while no temperature dependence was seen in the layers with higher Mn content. This can be explained by the metallic screening of the Mn ions, which prevents positron trapping at the hydrogenic states around Mn at high Mn content. The changes in the annihilation parameters above room temperature are very small in all the measured layers. The Ga vacancy concentrations in the $\text{Ga}_{1-x}\text{Mn}_x\text{As}$ layers are presented in Fig. 4.1. It is clearly seen that the Ga vacancy concentration decreases with increasing Mn concentration from $2 \times 10^{18} \text{ cm}^{-3}$ in the undoped LT GaAs to $4 \times 10^{16} \text{ cm}^{-3}$ in the $\text{Ga}_{1-x}\text{Mn}_x\text{As}$ layers with Mn content above 1 %.

According to theoretical calculations [68], the electronic part of the formation energy of the acceptor-type Ga vacancy increases and of the donor-type As antisite decreases when the Fermi level approaches the valence band. In our experiments this thermodynamical trend is observed as the decrease of the Ga vacancy concentration and increase of the As antisite concentration with increasing Mn content (Fig. 4.1). In $\text{Ga}_{1-x}\text{Mn}_x\text{As}$ with high Mn content the Fermi level is very close to the valence band. The theory then predicts that the Ga vacancies should be neutral and the As antisites should be in doubly positive charge state [68]. In this situation the difference of the formation energies of the two defects is about 2.5 – 3.5 eV [68]. Assuming that the defect concentrations in the LT-MBE grown layers are determined by the thermodynamical equilibrium, the difference of the formation energies can be determined from Fig. 4.1 as $E_F^{\text{VGa}} - E_F^{\text{AsGa}} = kT \ln([\text{As}_{\text{Ga}}]/[\text{V}_{\text{Ga}}]) \simeq 200 - 400 \text{ meV}$. This value is significantly smaller than that obtained from the theory, indicating that the absolute defect concentrations are determined by growth kinetics rather than by thermodynamical equilibrium. This holds especially for the Ga vacancy concentration, which increases when the As_2 flux at growth is increased, the effect being stronger with lower Mn content.

The As antisite concentrations in the $\text{Ga}_{1-x}\text{Mn}_x\text{As}$ layers are large enough to be significant for the compensation of the Mn acceptors and thus to affect the magnetic properties both through compensation and magnetic coupling [69, 70]. They are, however, too low to explain all of the self-compensation of the material. In similar layers, the Mn interstitial concentration has been estimated to be around 15 % of the total Mn concentration [71]. By adding the effect of these two types of defects together the total electrical compensation of the Mn doping can be explained.

The magnetic properties of the layers can be significantly improved by low temperature annealing due to the redistribution of Mn in the lattice [61, 72, 73]. Ga vacancies have been proposed to have an active role in the clustering of As antisites and substitutional Si in LT GaAs [55–59]. Their presence, especially at concentra-

tions significantly higher than expected from the thermodynamical equilibrium, may also affect the Mn diffusion by the vacancy mechanism in the Ga sublattice, particularly since Ga vacancies are mobile at the typical growth and annealing temperatures around 250 °C [74].

4.2 Future: Doping of GaN and ZnO with Mn

The drawback of (Ga,Mn)As is that the highest reported Curie temperatures do not exceed 200 K. ZnO and GaN have been predicted [52] on the basis of a Zener model to exhibit ferromagnetism above room temperature when doped with Mn. In addition, both GaN and ZnO are well-known piezoelectric and optoelectronic materials, and therefore incorporation of ferromagnetism in them can lead to a variety of new multifunctional phenomena.

The theoretical predictions on the above room temperature ferromagnetism in GaN and ZnO have initiated intensive experimental work (see, *e.g.*, Ref. [75] and the references therein). Positron annihilation studies have also been initiated on thin MOCVD-grown (Ga,Mn)N films and thick (Zn,Mn)O bulk single crystals grown by chemical vapor transport (CVT). The preliminary results show the presence of Ga vacancies in (Ga,Mn)N and Zn vacancies in (Zn,Mn)O. Interestingly, the addition of Mn into CVT-grown ZnO seems to suppress the formation of other point defects.

Chapter 5

Summary

In this work the thermodynamics and kinetics of vacancy defects in GaN, ZnO and (Ga,Mn)As were studied by positron annihilation spectroscopy. Both fast and moderated positrons were used in the studies of thick samples and thin overgrown layers. Measurements of positron lifetime and Doppler broadening of the 511 keV annihilation line were performed. In addition, we conducted optical measurements in the GaN and (Ga,Mn)As samples and electrical measurements in ZnO.

We demonstrate that in GaN the growth polarity has a crucial impact on the formation of Ga vacancies and vacancy clusters, which are more abundant at the N polar side. The concentrations of oxygen and of acceptor-type impurities are similarly correlated with the polarity, manifesting the importance of growth kinetics on defect formation. The vacancy concentrations are similar in both HVPE and high-pressure grown GaN in spite of the much higher growth temperature of the latter, which suggests that the thermal stability of the point defect complexes is an important factor determining which defects survive the cooling down from the growth temperature.

We show that the Zn vacancy is the dominant intrinsic acceptor in undoped ZnO, as expected from the theoretical considerations and thermodynamics. We also show that 2-MeV electron irradiation at room temperature produces vacancies on both sublattices and negative ion type defects, tentatively identified as O interstitials. The Zn vacancies and the negative ions act as compensating centers, both produced at concentrations $[V_{\text{Zn}}] \simeq c_{\text{st}} \simeq 2 \times 10^{16} \text{ cm}^{-3}$. These concentrations are smaller by a factor of about 30 than those obtained for the Ga vacancies in similar irradiation of GaN, which is a manifestation of the radiation hardness of ZnO. The irradiation-induced O vacancies are produced at a concentration of $[V_{\text{O}}] \simeq 3 \times 10^{17} \text{ cm}^{-3}$, indicating that *they* are the primary irradiation-induced defect instead of the Zn vacancies. In addition, we find that the irradiation-induced

Zn vacancies have an ionization level close to 2.3 eV, hence it is likely that they are involved in the transition responsible for the green luminescence in ZnO. We also studied the stability of the irradiation-induced defects. They fully recover after the annealing at 600 K. The Zn vacancies anneal out of the material in two stages, indicating that the Zn vacancies are parts of two different defect complexes. The O vacancies anneal simultaneously with the Zn vacancies at the later stage. The negative ion type defects anneal out between the two annealing stages of the Zn and O vacancies.

We show that Zn vacancies are the dominant defects observed by positrons in thin heteroepitaxial MOCVD ZnO layers. Their concentration depends on the surface plane of sapphire over which the ZnO layer has been grown. We show a correlation between the misorientation of the sapphire surface planes and the concentration of the vacancies for layers with thickness at most 500 nm. This correlation disappears for thicker layers. Moreover, the defect content in the layer depends on the layer thickness, and is larger closer to the interface.

We show that the concentrations of both native As antisites (donors) and Ga vacancies (acceptors) vary as a function of the Mn content in LT-MBE (Ga,Mn)As, following thermodynamic trends, but the absolute concentrations are determined by the growth kinetics and stoichiometry. The As antisite concentrations are significant for the hole compensation and magnetic properties. In addition, the presence of the Ga vacancies in the lattice with a concentration higher than that expected from thermodynamical considerations may enhance the diffusion of Mn in the Ga sublattice.

Bibliography

- [1] P. Y. Yu and M. Cardona, *Fundamentals of Semiconductors* (Springer-Verlag, Berlin Heidelberg, 1996).
- [2] S. Perkowitz, *Optical Characterization of Semiconductors* (Academic Press, London, 1993).
- [3] K. Saarinen, P. Hautojärvi, and C. Corbel, in *Identification of Defects in Semiconductors*, edited by M. Stavola (Academic Press, New York, 1998), p. 209.
- [4] K. Saarinen, in *III-V Nitride Semiconductors: Electrical, Structural and Defects Properties*, edited by M. O. Manasreh (Elsevier, Amsterdam, 2000), p. 109.
- [5] M. J. Puska and R. M. Nieminen, Rev. Mod. Phys **66**, 841 (1994).
- [6] J. Oila, J. Kivioja, V. Ranki, K. Saarinen, D. C. Look, R. J. Molnar, S. S. Park, S. K. Lee, and J. Y. Han, Appl. Phys. Lett. **82**, 3433 (2003).
- [7] K. Saarinen, P. Hautojärvi, J. Keinonen, E. Rauhala, J. Räisänen, and C. Corbel, Phys. Rev. B **43**, 4249 (1991).
- [8] H. Kauppinen, C. Corbel, K. Skog, K. Saarinen, T. Laine, P. Hautojärvi, P. Desgardin, and E. Ntsoenzok, Phys. Rev. B **55**, 9598 (1997).
- [9] M.-F. Barthe, L. Henry, C. Corbel, G. Blondiaux, K. Saarinen, P. Hautojärvi, E. Hugonnard, L. Di Cioccio, F. Letertre, and B. Ghyselen, Phys. Rev. B **62**, 16638 (2000).
- [10] A. J. Ptak, L. J. Holbert, L. Ting, C. H. Schwartz, M. Moldovan, N. C. Giles, T. H. Myers, P. Van Lierde, C. Tian, R. A. Hockett, S. Mitha, A. E. Wickenden, D. D. Koleske, and R. L. Henry, Appl. Phys. Lett **79**, 2740 (2001).

- [11] M. Rummukainen, J. Oila, A. Laakso, K. Saarinen, A. J. Ptak, and T. H. Myers, *Appl. Phys. Lett.* **84**, 4887 (2004).
- [12] S. F. Chichibu, A. Setoguchi, A. Uedono, K. Yoshimura, and M. Sumiya, *Appl. Phys. Lett.* **78**, 28 (2001).
- [13] I. Arslan and N. D. Browning, *Phys. Rev. Lett.* **91**, 165501 (2003).
- [14] J. Karpinski, J. Jun, and S. Porowski, *J. Crystal Growth* **66**, 1 (1984).
- [15] M. Leszczynski, I. Grzegory, H. Teisseyre, T. Suski, M. Bockowski, J. Jun, J. M. Baranowski, S. Porowski, and J. Domagala, *J. Crystal Growth* **169**, 235 (1996).
- [16] D. C. Look, C. E. Stutz, R. J. Molnar, K. Saarinen, and Z. Liliental-Weber, *Solid State Commun.* **117**, 571 (2001).
- [17] M. Bockowski, I. Grzegory, S. Krukowski, B. Lucznik, Z. Romanowski, M. Wroblewski, J. Borysiuk, J. Weyher, P. Hageman, and S. Porowski, *J. Crystal Growth* **246**, 194 (2002).
- [18] Z. Liliental-Weber, J. Jasinski, and J. Washburn, *J. Crystal Growth* **246**, 259 (2002).
- [19] K. Saarinen, J. Nissilä, P. Hautojärvi, J. Likonen, T. Suski, I. Grzegory, B. Lucznik, and S. Porowski, *Appl. Phys. Lett.* **75**, 2441 (1999).
- [20] E. Frayssinet, W. Knap, S. Krukowski, P. Perlin, P. Wisniewski, T. Suski, I. Grzegory, and S. Porowski, *J. Crystal Growth* **230**, 442 (2001).
- [21] K. Saarinen, T. Laine, S. Kuisma, J. Nissilä, P. Hautojärvi, L. Dobrzynski, J. M. Baranowski, K. Pakula, R. Stepniewski, M. Wojdak, A. Wysmolek, T. Suski, M. Leszczynski, I. Grzegory, and S. Porowski, *Phys. Rev. Lett.* **79**, 3030 (1997).
- [22] Z. Liliental-Weber, M. Benamara, J. Washburn, I. Grzegory, and S. Porowski, *Phys. Rev. Lett.* **83**, 2370 (1999).
- [23] Z. Liliental-Weber, M. Benamara, W. Swider, J. Washburn, I. Grzegory, S. Porowski, D. J. H. Lambert, C. J. Elting, and R. D. Dupuis, *Appl. Phys. Lett.* **75**, 4159 (1999).
- [24] S. Hautakangas, J. Oila, M. Alatalo, K. Saarinen, L. Liskay, D. Seghier, and H. P. Gislason, *Phys. Rev. Lett.* **90**, 137402 (2003).
- [25] Z. Liliental-Weber and D. Cherns, *J. Appl. Phys.* **89**, 7833 (2001).

- [26] J. Neugebauer and C. G. Van de Walle, *Appl. Phys. Lett.* **69**, 503 (1996).
- [27] T. Paskova, P. P. Paskov, E. Valcheva, V. Darakchieva, J. Birch, A. Kasic, B. Arnaudov, S. Tungasmita, and B. Monemar, *phys. stat. solidi (a)* **201**, 2265 (2004).
- [28] K. Saarinen, T. Suski, I. Grzegory, and D. C. Look, *Phys. Rev. B* **64**, 233201 (2001).
- [29] Y. V. Gorelkinskii and G. D. Watkins, *Phys. Rev. B* **69**, 115212 (2004).
- [30] D. Galland and A. Herve, *Solid State Commun.* **14**, 953 (1974).
- [31] D. Galland and A. Herve, *Phys. Lett.* **33A**, 1 (1970).
- [32] K. Leutwein and J. Schneider, *Z. Naturf.* **26a**, 1236 (1971).
- [33] A. L. Taylor, G. Filipovich, and G. K. Lindeberg, *Solid State Commun.* **8**, 1359 (1970).
- [34] J. M. Smith and W. E. Vehse, *Phys. Lett.* **31A**, 147 (1970).
- [35] C. Gonzales, D. Galland, and A. Herve, *Phys. Stat. Solidi (b)* **72**, 309 (1975).
- [36] L. S. Vlasenko and G. D. Watkins, *Phys. Rev. B* **71**, 125210 (2005).
- [37] D. C. Reynolds, D. C. Look, B. Jogai, and H. Morkoc, *Solid State Comm.* **101**, 643 (1997).
- [38] A. F. Kohan, G. Ceder, D. Morgan, and C. G. Van de Walle, *Phys. Rev. B* **61**, 15019 (2000).
- [39] K. Vanheusden, C. H. Seager, W. L. Warren, D. R. Tallant, and J. A. Voight, *Appl. Phys. Lett.* **68**, 403 (1995).
- [40] K. Vanheusden, W. L. Warren, C. H. Seager, D. R. Tallant, J. A. Voight, and B. E. Gnade, *J. Appl. Phys.* **79**, 7983 (1996).
- [41] H.-J. Egelhaaf and D. Oelkrug, *J. Crystal Growth* **161**, 190 (1996).
- [42] D. C. Look, D. C. Reynolds, J. W. Hemsky, R. L. Jones, and J. R. Sizelove, *Appl. Phys. Lett.* **75**, 811 (1999).
- [43] A. Y. Polyakov, N. B. Smirnov, A. V. Govorkov, A. E. Kozhukova, V. I. Vdovin, K. Ip, M. E. Overberg, Y. W. Heo, D. P. Norton, S. J. Pearton, J. M. Zavada, and V. A. Dravin, *J. Appl. Phys.* **94**, 2895 (2003).
- [44] D. C. Look, D. C. Reynolds, J. R. Sizelove, R. L. Jones, C. W. Litton, G. Cantwell, and W. C. Harsch, *Solid State Commun.* **105**, 399 (1998).

- [45] D. C. Look, J. W. Hemsky, and J. R. Sizelove, *Phys. Rev. Lett.* **82**, 2552 (1999).
- [46] M. Hakala, M. J. Puska, and R. M. Nieminen, *Phys. Rev. B* **57**, 7621 (1998).
- [47] M. J. Puska, C. Corbel, and R. M. Nieminen, *Phys. Rev. B* **41**, 9980 (1990).
- [48] J. Mäkinen, C. Corbel, P. Hautojärvi, P. Moser, and F. Pierre, *Phys. Rev. B* **39**, 10162 (1989).
- [49] C. Munuera, J. Zuñiga-Pérez, J. F. Rommeluere, V. Sallet, R. Triboulet, F. Soria, V. Muñoz-San José, and C. Ocal, *J. Crystal Growth* **264**, 70 (2004).
- [50] J. K. Furdyna, *J. Appl. Phys.* **64**, R29 (1988).
- [51] H. Ohno, *J. Magn. Magn. Mater.* **200**, 110 (1999).
- [52] T. Dietl, H. Ohno, F. Matsukura, J. Cibert, and D. Ferrand, *Science* **287**, 1019 (2000).
- [53] T. Dietl, H. Ohno, and F. Matsukura, *Phys. Rev. B* **63**, 195205 (2001).
- [54] T. Jungwirth, J. Sinova, K. Y. Wang, K. W. Edmonds, R. P. Campion, B. L. Gallagher, C. T. Foxon, Q. Niu, and A. H. MacDonald, *Appl. Phys. Lett.* **83**, 320 (2003).
- [55] J. Gebauer, R. Krause-Rehberg, S. Eichler, M. Luysberg, H. Sohn, and E. R. Weber, *Appl. Phys. Lett.* **71**, 638 (1997).
- [56] M. Luysberg, H. Sohn, A. Prasard, P. Specht, Z. Liliental-Weber, E. R. Weber, J. Gebauer, and R. Krause-Rehberg, *J. Appl. Phys.* **83**, 561 (1997).
- [57] T. Laine, K. Saarinen, P. Hautojärvi, C. Corbel, and M. Missous, *J. Appl. Phys.* **86**, 1888 (1999).
- [58] J. Gebauer, F. Börner, R. Krause-Rehberg, T. E. M. Staab, W. Bauer-Kugelman, G. Kögel, W. Triftshäuser, P. Specht, R. C. Lutz, E. R. Weber, and M. Luysberg, *J. Appl. Phys.* **87**, 8368 (2000).
- [59] J. Gebauer, R. Zhao, P. Specht, E. R. Weber, F. Börner, F. Redmann, and R. Krause-Rehberg, *Appl. Phys. Lett.* **79**, 4313 (2001).
- [60] F. Tuomisto, J. Slotte, K. Saarinen, and J. Sadowski, *Acta Phys. Pol. A* **103**, 601 (2003).
- [61] J. Sadowski and J.Z. Domagala, *Phys. Rev. B* **69**, 075206 (2004).

- [62] P. Silverberg, G. Omling, and L. Samuelson, Appl. Phys. Lett. **52**, 1689 (1988).
- [63] G. Vincent, D. Bois, and A. Chantre, J. Appl. Phys. **55**, 3643 (1982).
- [64] S. K. Brierley and D. S. Lehr, Appl. Phys. Lett. **55**, 2426 (1989).
- [65] M. Haiml, U. Siegner, F. Morier-Genoud, U. Keller, M. Luysberg, R. C. Lutz, P. Specht, and E. R. Weber, Appl. Phys. Lett. **74**, 3134 (1999).
- [66] K. Saarinen, P. Hautojärvi, P. Lanki, and C. Corbel, Phys. Rev. B **44**, 10585 (1991).
- [67] J. Gebauer, M. Lausmann, T. E. M. Staab, R. Krause-Rehberg, M. Hakala, and M. J. Puska, Phys. Rev. B **60**, 1464 (1999).
- [68] J. E. Northrup and S. B. Zhang, Phys. Rev. B **47**, 6791 (1993).
- [69] P. A. Korzhavyi, I. A. Abrikosov, E. A. Smirnova, L. Bergqvist, P. Mohn, R. Mathieu, P. Svedlindh, J. Sadowski, E. I. Isaev, Y. K. Vekilov, and O. Eriksson, Phys. Rev. Lett. **88**, 187202 (2002).
- [70] S. Sanvito and N. A. Hill, Appl. Phys. Lett. **78**, 3493 (2001).
- [71] K. M. Yu, W. Walukiewicz, T. Wojtowicz, I. Kuryliszyn, X. Liu, Y. Sasaki, and J. K. Furdyna, Phys. Rev. B **65**, 201303(R) (2002).
- [72] K. Edmonds, P. Boguslawski, K. Y. Wang, R. P. Campion, S. N. Novikov, N. R. S. Farley, B. L. Gallagher, C. T. Foxon, M. Sawicki, T. Dietl, M. Buongiorno Nardelli, and J. Bernholc, Phys. Rev. Lett. **92**, 037201 (2004).
- [73] B. J. Kirby, J. A. Borchers, J. J. Rhyne, S. G. E. te Velthuis, A. Hoffmann, K. V. O'Donovan, T. Wojtowicz, X. Liu, W. L. Lim, and J. K. Furdyna, Phys. Rev. B. **69**, 081307(R) (2004).
- [74] C. Corbel, F. Pierre, K. Saarinen, P. Hautojärvi, and P. Moser, Phys. Rev. B **45**, 3386 (1992).
- [75] S. J. Pearton, C. R. Abernathy, G. T. Thaler, R. M. Frazier, Y. H. Heo, M. Ivill, D. P. Norton, and Y. D. Park, Defect Diffus. Forum **230-232**, 17 (2005).